学位論文

Geological study on saturnian small
satellites: Implications to
ephemeral cryovolcanism of Enceladus

（土星系小型衛星に記録された
エンセラダスの火山活動）

平成 26 年 12 月博士（理学）申請

東京大学理学系研究科
地球惑星科学専攻
平田　直之

Doctorate Thesis

Geological study on saturnian small satellites: Implications to ephemeral cryovolcanism of Enceladus

December 2014

Graduate School of Science, The University of Tokyo

Department of Earth and Planetary Science

Naoyuki Hirata

Abstract

The cryovolcanism of Enceladus should have been less active than at present otherwise the global shape of the satellite would display significant clues indicative of such a high discharge rate over billions of years. However, the exact estimate of the duration of current cryovolcanism is almost impossible from geological observations of Enceladus alone because its high activity erases previous records. For this reason, I study small satellites near Enceladus rather than directly study the surface of Enceladus; I focus on the interaction between these satellites and the E-ring because Enceladus generates plumes composed of gas and particles, which forms Saturn's tenuous E-ring. I have identified diverse evidence indicating that the E-ring particles accumulate on the small satellites, such as Helene, Telesto, Calypso, Methone, and Pallene, which have received little attention by science community until now. Nevertheless, high-resolution images of the satellites have been obtained during the past decade through the Cassini mission. Especially, nearly the entire surface of Helene has been imaged in high-resolution, which enables me to preform detailed investigation of its geological features. Based on the images of Helene, I have developed a shape model, measured the distribution of craters, and examined geological features. As a result, I find that the E-ring particles have accumulated preferentially on the leading hemisphere of Helene, which results in the deficiency of small craters as well as the development of numerous streaky depressions formed by mass movement. Furthermore, I find that Telesto, Calypso, Methone, and Pallene have spherical shapes with unusually smooth surfaces, which can also be explained by the accumulation of the E-ring particles. Finally, I conclude that the ages of the E-ring deposits on the small satellites are likely to be at most 100 Ma. This collectively indicates that the cryovolcanic activity currently occurring on Enceladus is ephemeral.

Contents

Contents

Figure

Contents

Table

Introduction

The giant planet Saturn has more than 50 officially-named satellites. Their sizes range from Titan (with a diameter of 5152 km) to Aegaeon (~0.5 km), and therefore, the satellites exhibit a wide diversity. Here I divided saturnian satellites into a few classes: small satellites (with radii < 100 km), such as Pan, Atlas, Pandora, Prometheus, Janus, Epimetheus, Methone, Pallene, Telesto, Calypso, and Helene and mid-sized satellites (with radii < 800 km), such as Mimas, Enceladus, Tethys, Dione, and Rhea. The mid-sized satellites commonly present a nearly spherical shape in hydrostatic equilibrium while the small satellites have an irregular shape.

Saturn's small satellites are suitable to study the geology on small satellites of giant planets. This is because small satellites were not imaged at sufficient resolution for geological examinations before the Cassini spacecraft encountered at Saturn. Voyager 1, 2 and Galileo spacecraft have obtained the images of Jupiter's small satellites, Metis, Amalthea, and Thebe, Uranus' satellite, Puck, and Neptune's satellite, Larissa, which allow showing an irregular shape with heavily-cratered surface while the geological features except for large craters are difficult to be distinguished. I note that other small satellites are imaged at only a dot. On the other hand, Cassini observations in the last decade have acquired numerous high-resolution images of saturnian small satellites: for example, 437 images for Helene (500 m/pixel to 24 m/pixel), 208 images for Janus (2 km/pixel to 170 m/pixel), and 64 images for Epimetheus (1km/pixel to 220 m/pixel). Interestingly, the results up to now imply that the geology of the small satellites presents curious phenomena unlike that of mid-sized satellites or asteroids.

Previous studies proposed that the formation and evolution of saturnian small satellites were much different from those of mid-sized satellites. Pan, Atlas, Prometheus, and Pandora have been formed by the accumulations of the A-ring (e.g. Porco et al. 2007). This is evidenced by (i) their densities, which imply their structures are a rubble pile (Porco et al. 2007), (ii) their volumes, which fill the Roche lobes of the satellites (Porco et al. 2007), (iii)

their disk-like shapes, which are made of ring particles swept up by the satellites (Charnoz et al. 2007), and (iv) their spectra similar to A-ring (Filacchione et al. 2010, Buratti et al. 2010). Janus and Epimetheus are originated from aggregates of the breccia after a larger satellite has been disrupted in early Saturn system, which is suggested by (i) the low densities, which is almost the same as each other (~0.63 g/cm^3) and (ii) the surface features, which resemble each other (Stooke 1993, Stooke and Lumsdon 1993). Over all, small satellites may have been formed by disruption and re-accretion rather than originated from saturnian subnebula (Johnson and Estrada 2009).

Also, the morphologies of the small satellites are much different from those of asteroids, whereas many small satellites are expected to have the environment similar to asteroids in terms of the tiny gravity and the absence of the endogenic process. Asteroids, such as Gaspra, Ida, Mathilde, Eros, Itokawa, and Vesta, have been observed by several spacecraft, which reveal varieties of small bodies in terms of their characteristics, formation processes, chemical compositions, surface processes, and so on. Interestingly, the surface morphologies of the asteroids are dominated by not only impact cratering but also seismic shaking, igneous process, or global sorting processes (e.g. Sullivan et al. 2002, Richardson et al. 2004, Miyamoto et al. 2007, Zuber et al. 2011). Saturnian small satellites also appear unique features dissimilar to asteroids, for example, a smooth surface on Atlas, streaky depressions on Helene, spherical shapes of Methone and Pallene, or pond-like deposits on Janus and Epimetheus.

These examples indicate the small satellites have likely evolved in their own particular ways, unlike mid-sized satellites and asteroids. Hence, the small satellites can contribute to enhance for our understanding of small bodies and will provide a clue to understand the history of Saturn system, including Saturn itself. Based on this view, I carefully study geological features of saturnian small satellites, using the newly-developed shape models, image analyses, mapping the surface features, or numerical simulation. I subdivided this thesis into three parts; the research of Helene in

Part 1, Atlas in Part 2, and Janus and Epimetheus in Part 3.

As a result, I conclude that the interaction between satellites and ring materials play an important role to surface processes on the small satellites. Until now, the surfaces of satellites are known to be influenced by rings, for example, hemispheric albedo dichotomies on mid-sized satellites in E-ring (Buratti and Veverka 1984, Ostro et al. 2010, Verbiscer et al. 2007). However, the surface alternations are limited to be surficial phenomenon with sub-micron in depth. Contrary, small satellites appear thick deposits of ring materials, which cause the unique features of the small satellites, as shown in the following parts.

This result implies that small satellites significantly record the history of Saturn's ring system. This is because ring systems are generally ephemeral (for example, E-ring particles are as old as 8 years (Ingersoll et al. 2011)) while the deposits of ring particles lying on small satellites are expected to have much more stable. I show a best example to discuss the lifetime of cryovolcanism on Enceladus based on the surface of small satellites in Part 1. Part 1 includes main results and discussions of this thesis. I note that the contents of Part 1 and Part 2 have been published in Hirata et al. (2014) and Hirata and Miyamoto (2012), respectively.

Part 1
1. Satellites of the E-ring
1.1. The endogenic activity of Enceladus

Enceladus, with 252 km in radius, is one of saturnian satellites. Despite of its small size, Enceladus has the endogenic activity. This is suggested by geyser-like plumes composed of icy particles and water vapor (Kargel 2006), which are discovered by the Cassini spacecraft in 2005. The mean density of Enceladus is 1609 kg/m^3, which indicates that Enceladus has an icy mantle with a rocky core (e.g. Matson et al. 2009). In addition, possible interior structure in Enceladus is suggested to contain a subsurface ocean (Porco et al. 2006a). A primary thermal source of the activity is generated by tidal heating and radioactive decay (e.g. Spencer et al. 2009).

Previous studies suggest that Enceladus has not been active at its current level. First, Kargel (2006) shows that no geological evidence exists to support a large change in its radius, which would be expected if the current mass-loss rates have been maintained. Second, Roberts and Nimmo (2008) shows that the current energy output of Enceladus is difficult to sustain over Solar System history. Third, Enceladus' current heat flux greatly exceeds that occurring in equilibrium with its current eccentricity given the time-averaged Q of Saturn (Meyer and Wisdom 2007), suggesting that the current activity may be greater than average. Finally, recent global geophysical models show that Enceladus can exhibit episodic activity, with short periods of intense activity interspersed with long quiescent epochs (Showman et al. 2013).

Those studies imply that the cryovolcanism on Enceladus has not been maintained over Solar System history, however, its age is unclear. This is partly because the crater chronology is not adaptable on Enceladus. In other word, the crater density on Enceladus does not directly indicate when Enceladus' cryovolcanism has begun but shows a state of dynamic equilibrium between the cratering and resurfacing rates. Instead of Enceladus, I focus on

other satellites in the E-ring and examine the E-ring deposits on the satellites. Because the E-ring is considered to be originated from the cryovolcanism of Enceladus (Kempf et al. 2008), surfaces of satellites in the E-ring region have an important clue to understand the endogenic history of Enceladus.

1.2. The E-ring and accumulation on satellites

Saturn's E-ring is a wide tenuous ring system, beginning beyond Mimas and ending around Titan (Kempf et al. 2008). There are 5 mid-sized satellites in the E-ring; Mimas, Enceladus, Tethys, Dione, and Rhea (Fig. 1). The mid-sized satellites have been observed at high resolution by the Cassini spacecraft. The E-ring material has obviously been accumulated on their surfaces. For example, the leading hemispheres of Dione and Tethys are 1.8 times and 1.1 times, respectively, brighter than their trailing hemispheres (Buratti and Veverka 1984). The dichotomies have been suggested to result from differential accumulation of E-ring material on their surfaces (Ostro et al. 2010, Verbiscer et al. 2007). However, no depositional features have been reported on the satellites in the E-ring region except for those on Enceladus (e.g. buried craters) (Kirchoff and Schenk 2009). Contrary, small satellites, such as Telesto, Calypso, and Helene, likely retain more information of the E-ring because of the absence of the endogenic process. I thoroughly examine all high-resolution images obtained by the Cassini spacecraft through November 2013. As a result, I find that possible depositional features ubiquitously exist on the small satellites.

1.3. Small satellites in the E-ring region

There are 7 small satellites in this region (Fig. 1, Table 1). Among them, Methone, Pallene, Telesto, Calypso, and Helene have been observed at relatively high resolution by the Cassini spacecraft. Anthe and Polydeuces are not imaged at sufficient resolution to examine their surface features. Cassini observation also reveals their detailed orbital elements (Jacobson et al. 2008), sizes (Porco et al. 2007), surface features (Thomas et al. 2013), and spectra (Buratti et al. 2010, Filacchione et al. 2010), though their masses and densities are still unknown. Visual and infrared spectra of these small satellites indicate that their surfaces appear to be

covered by the E-ring material (Filacchione et al. 2013). Thus, the surface features may hold an important key to understand the possible influence of the E-ring material.

Pallene and Methone, discovered in 2004 from images obtained by the Cassini spacecraft (Porco et al. 2005), are satellites known as the Alkyonides, located within Enceladus. The highest-resolution image obtained for Pallene (Fig. 2G) shows only its outline (Fig. 2G). High-resolution images have been obtained for Methone (Fig 2H), which show only part of the leading hemisphere.

Telesto and Calypso (Fig. 2E, F), discovered in 1980 from Earth-based observations (Seidelmann et al. 1981), are located at L4 and L5 points of Tethys, respectively. Although high-resolution images are obtained for these satellites, their areal coverage is limited; only parts of leading and tailing sides for Telesto and Calypso.

Helene, also discovered in 1980 from Earth-based observation (Lecacheux et al. 1980), is located at L4 point of Dione. Different from satellites discussed above, many high-resolution images have been obtained for Helene during several Cassini's flybys (Fig. 2A-D, 3). Therefore, I can study the geological features of Helene based especially on high-resolution images.
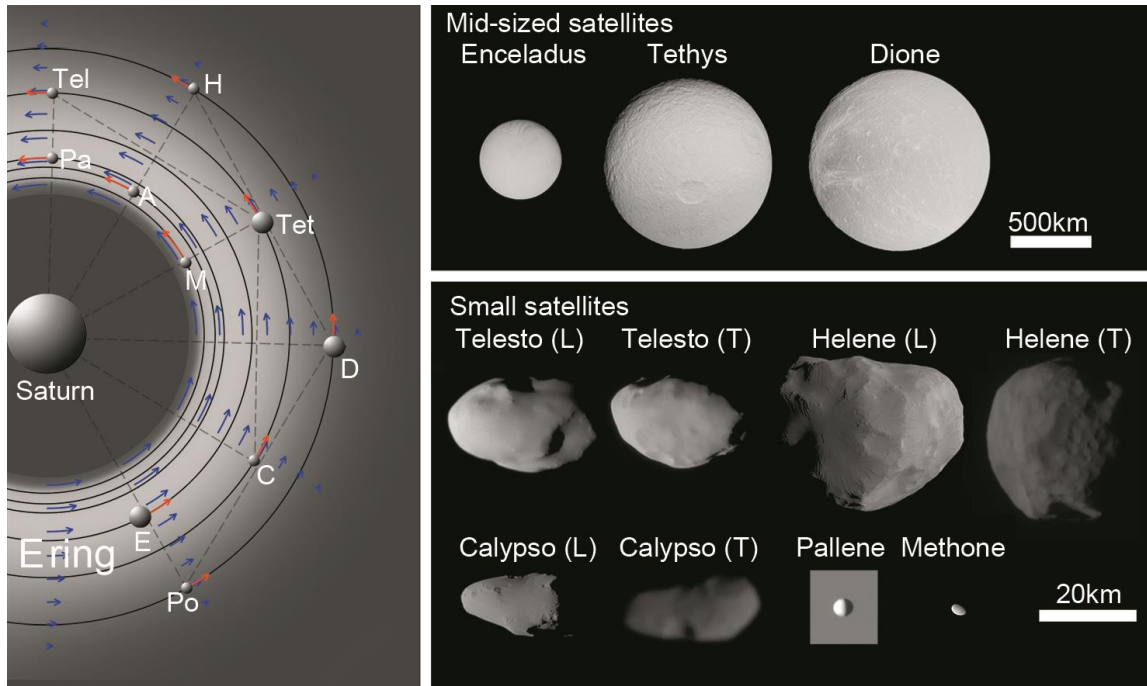
Figure 1 Satellites of the E-ring

(left) Conceptual figure showing orbits of satellites in the E-ring region (brighter color in the background). Three mid-sized satellites and seven small satellites are shown. Red and blue arrows indicate relative velocities of satellites and E-ring particles (see text), respectively. Note that the velocity of both satellites and the E-ring particles are faster in inner orbits. Mid-sized (right upper) and small (right lower) satellites located at the E-ring region shown in the same scales. (L) and (T) indicate that the image is the leading and the trailing side, respectively. For this image, I use N1495319334, N1546295078, W1649316019, N168712110, N1563643679, N1630076968, N1514163666, N1644754662, N1506184171, N1665947247, and N00189072.

Table 1 Satellites in the E-ring region.

	Semi-major axis （km）	Mean-radius （km）
Mimas	185,539	198
Methone	194,440	1.6±0.6
Anthe	197,700	~1.0
Pallene	212,280	2.2±0.3
Enceladus	237,948	252
Tethys	294,619	531
Telesto	294,710	12.4±0.4
Calypso	294,710	10.6±0.7
Dione	377,396	561
Polydeuces	377,200	1.3±0.4
Helene	377,420	16.5±0.6
Rhea	527,108	764
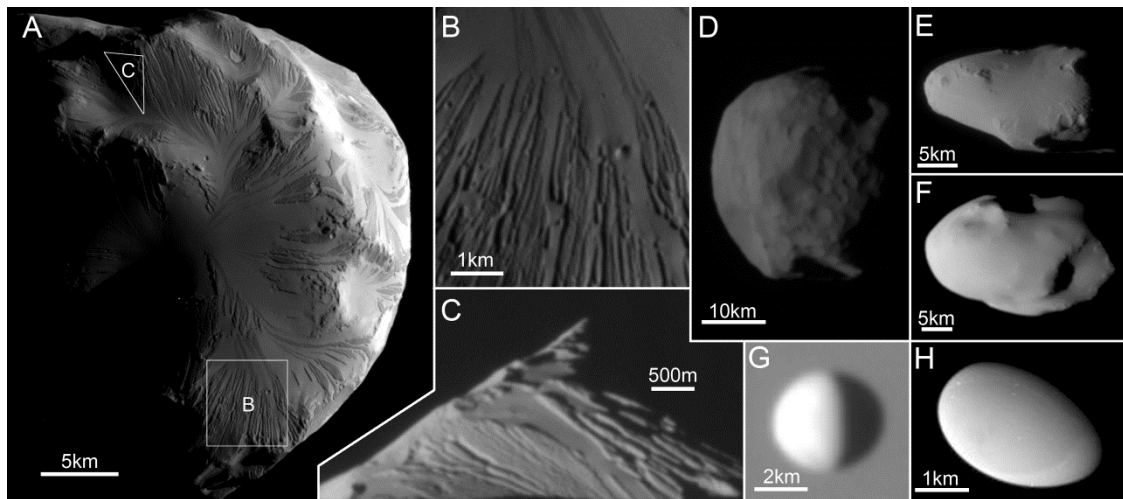
Figure 2 Small satellites in the E-ring.
(A) Helene's leading hemisphere (N1687119539). Insets indicate locations of (B) and (C). (B) Close-up image of the streaky depressions (N1687119539; 42 m/pixel). (C) The highest-resolution image of Helene (N1646317865; 24 m/pixel). (D) Helene's trailing hemisphere (N1563643679). (E) Calypso's leading hemisphere (N1644754662). (F) Telesto's leading hemisphere (N1630076968). (G) Anti-Saturn side of Pallene with Saturn as a background (N1665947247). (H) Methone's leading hemisphere (N00189072).

2. Geological studies of Helene

Through 7 flybys between 2006 and 2011, the Cassini spacecraft obtained 437 high-resolution images of Helene (500 m/pixel or better). All of the raw data are available for free via NASA's Planetary Data System (http://pds.nasa.gov/). Those images show Helene's non-uniform appearance. While sub-Saturn side of the trailing hemisphere shows numerous impact craters close to be saturated, the leading hemisphere appears to be generally smooth without small craters.

2.1. Shape model of Helene

For a critical evaluation of the distribution of craters and other geological features, estimate of areas for particular parts of the body are needed, which requires a shape model of Helene. Fortunately, high-resolution images aerially cover almost entire surface of Helene, except for relatively small regions at its north pole and trailing hemisphere (Fig. 3). Also, the aerial coverage of each image overlaps with at least one or two other images, which can be used as a stereo pair to develop a simple shape-model sufficient enough for the above purpose.

To develop a shape model, I follow a previously proposed method (Hartley and Zisserman 2004) by using 16 high-resolution images shown in Table 2 as follows; 1) Split the surface of Helene into 10 parts; 2) Select 3 images from the 16 high-resolution images showing a particular part of the body; 3) Identify at least 8 corresponding points in all of these 3 images (Fig. 3); 4) Measure both relative locations of these corresponding points and camera positions of 3 images using the epipolar geometry, which results in forming a local shape model. I perform the process of 2) to 4) for all 10 parts of Helene before binding the local shape models into a single very-rough shape model. Because the camera positions are now precisely determined, I perform stereo analyses for all of the 16 high-resolution images to increase the corresponding points, which results in obtaining exact locations of in total 750 points to improve the quality of the shape model. I compare the resultant shape model to all of the high-resolution images obtained by the Cassini

spacecraft to confirm that the shape model properly reproduces both outlines and features in these images.

Moreover, I calculate the local gravitational gradients for the entire surface of Helene. I constructed the numerical shape model as the assemblage of 7492 small tetrahedrons, whose densities were assumed to be the same. The leading hemisphere is specifically analyzed carefully by defining 1024 polygons. To derive the local gravity, I i) measure the distance between the geometric center of a single tetrahedron at the centroid of a given polygon; ii) calculate the gravitational vector from the distance and the volume of the tetrahedron; iii) perform i) and ii) for all tetrahedrons consisting of the shape model; iv) integrate these gravitational vectors obtained by iii) to obtain the total gravity acceleration from entire Helene at the given polygon; v) calculate the inner product between the normal vector of the polygon and the total gravitational vector on the polygon to obtain the angle of the slope; vi) remove the component along the normal vector of the polygon from the gravitational vector to obtain the direction of the local gravity on the polygon; vii) perform i) to vi) for all 1024 polygons consisting of the surface of leading hemisphere.

Assuming that the center of mass coincides with the geometric center of Helene, I also develop a topographic map of Helene based on the shape model (Fig. 4A and Table 3). This enables me to identify the existences of basins, which are divided by ridges. The north pole is located within a large depression, whose diameter is about or a little larger than 15 km. This is nearly equal to the mean radius of Helene, which makes the overall shape of Helene unevenly (the volume of equatorial regions far exceeds that of polar regions). The most stable axis, where the principal moment of inertia achieves the largest value for the geometry of Helene, is close to its actual rotation axis.

2.2. The distribution of craters on Helene

As observed on most satellites of Saturn, Helene has numerous craters. Using the high-resolution images, I identify more than 70 craters, which are not uniformly distributed over the surface of Helene. The distribution of identified craters is shown in

Fig. 5 and 6. Then, craters are identified by (i) a circular depression with a rim, (ii) a depression imaged with a resolution of at least 5 pixels for clear understanding of its shape, and (iii) a depression identified in more than one image. Larger craters (> 10 km) on north and south polar terrain are also verified by my shape model.

Based on the crater density, I can identify three distinct regions (Fig. 4B), whose crater size-frequency distributions in a relative plot (i.e. R-plot) are shown in Fig. 5. R-plot means the ratio of the differential form of cumulative crater-size distribution to a size-frequency distribution with differential slope equal to 3. Error bars are defined as $\pm R*N^{-0.5}$, where N is the number of craters between a bin. For these analyses, I follow the method of Crater Analysis Technique Working Group (1979).

The largest crater on Helene is probably the large depression at the north polar-region, whose diameter is ~15 km, if the depression is formed by a single crater. Other than this depression, at least 5 craters are larger than ~10 km in diameter and at least 8 craters are 5 to 10 km in diameter. They are almost uniformly distributed over the entire surface of Helene. Contrary, the number of small craters (below 5 km in diameter) varies significantly depending on regions; I identify three distinct regions based on the crater densities, such as (1) heavily cratered terrain (red in Fig. 4B), which covers the sub-Saturn side of the trailing hemisphere (I identify 38 craters ranging from 0.7 km to 10 km in diameter), (2) moderately cratered terrain (yellow in Fig. 4B), which covers the anti-Saturn side of the trailing hemisphere (22 craters ranging from 0.2 km to 12 km), and (3) less cratered terrain (blue in Fig. 4B), which covers the leading hemisphere (14 craters ranging from 1 km to 10 km). I note that crater identifications in the moderately cratered terrain suffered from low solar-incidence angles in most images of this region.

The high crater-density on the trailing hemisphere indicate that Helene is basically an old object; based on the crater chronology of Saturn system discussed in Zahnle et al. (2003), the surface age of the heavily cratered terrain on the trailing hemisphere may be estimated as older than ~1.0 Gy. Also, the

distribution of large craters (> 5 km) indicates that the age of Helene is older than ~1.0 Gy. These two estimates coincide very well, which likely supports the idea that the body of Helene itself is formed in the earlier Saturn system. On the other hand, the deficiency of craters on the leading hemisphere (blue region of Fig. 4B, consisting at least 33 % of the entire surface of Helene) indicates that a process of either erasing a crater or prohibiting to form a crater may be acting (or have been acting) on the leading hemisphere.

Table 2 Images used for developing the shape model of Helene.

Image	Date (UTC)	Range (km)	Res. (m)	Sub-Cassini		Sub-Solar	
				Lat.	Lon.	Lat.	Lon.
N1519536732	2006-2-25	67836	423.7	-0.4	96.6	-18.5	187.2
N1519537272	2006-2-25	68271	426.4	-0.4	93.6	-18.5	188.0
N1534480072	2006-8-27	50353	314.5	73.8	31.0	-16.2	237.9
N1534483492	2006-8-27	61949	387.0	75.4	138.9	-16.2	243.0
N1563643679	2007-7-20	38890	242.9	-2.5	316.2	-11.4	13.4
N1563644326	2007-7-20	38466	240.3	-2.6	321.6	-11.4	14.4
N1506207298	2008-11-24	69067	431.4	25.7	347.3	-3.9	329.6
N1646315085	2010-3-3	22073	137.9	-3.8	4.0	3.2	193.1
N1646319549	2010-3-3	18821	117.6	-3.6	183.0	3.2	199.9
N1646320608	2010-3-3	28482	177.9	-2.2	186.0	3.2	201.5
W1646317554	2010-3-3	1911	119.4	-42.4	116.4	3.2	196.9
W1646317899	2010-3-3	4113	256.9	-18.2	164.8	3.2	197.1
N1675165048	2011-1-31	31434	190.3	-3.5	114.3	8.2	173.3
N1687119135	2011-6-18	7355	44.5	2.7	147.3	10.1	19.2
N1687121104	2011-6-18	9800	59.3	1.3	87.4	10.1	22.2
N1687121464	2011-6-18	11031	66.8	1.0	81.8	10.1	22.8
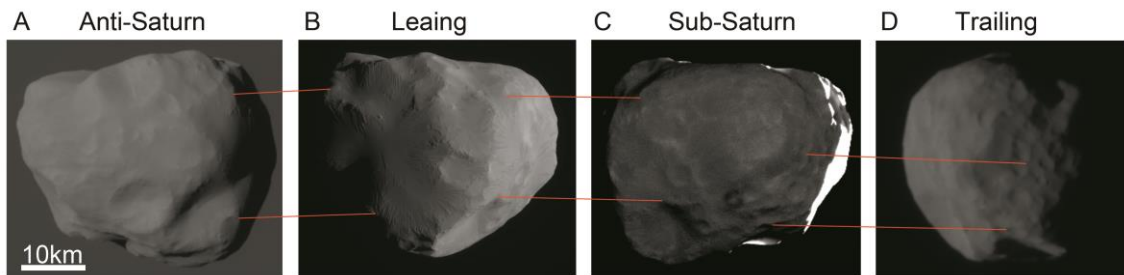
Figure 3 Images used for constructing the shape model.
Not all of them; see Table 2. Red lines connect the same signature points between images. (Image numbers from left to right, N1646319549, N1687121104, N1646315085, and N1563643679).
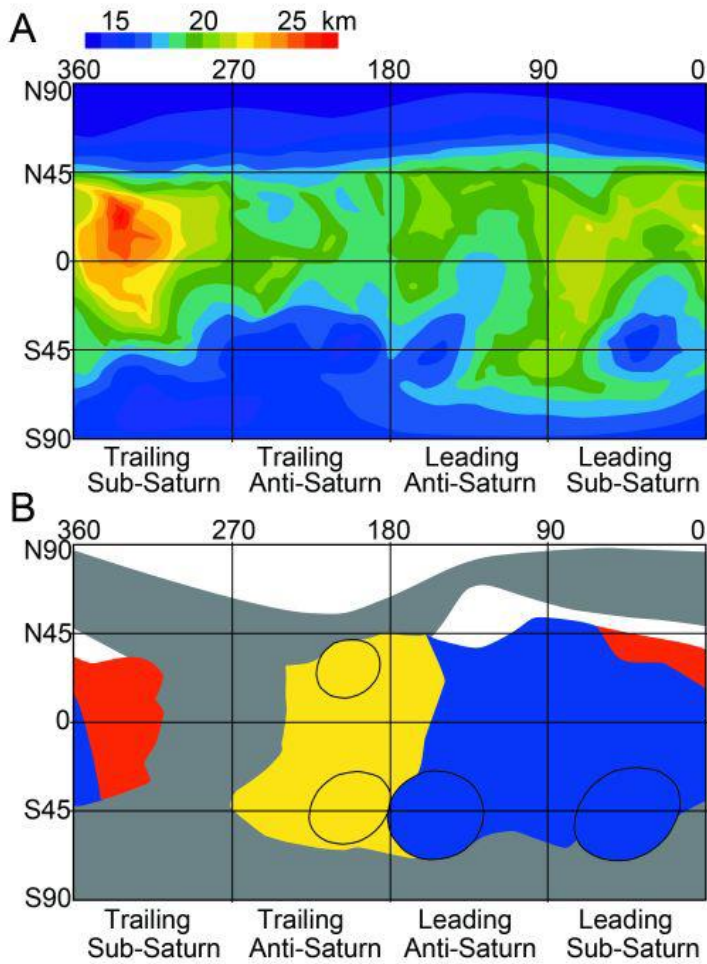
Figure 4 Topography and crater distribution of Helene.
(A) Global topographic map of Helene with colors representing topographic height relative to the geometric center. (B) Regional map with heavily cratered terrain (red), moderately cratered terrain (yellow), less cratered terrain (blue), features unidentified (gray), and no images obtained (white). Black circles indicate large craters (~10 km in diameter).

(a)

(b)

Figure 5 Crater size-frequency.
(a) The cumulative crater size-frequency distribution (km^{-2}) on Helene. (b) The relative size-frequency distribution of Helene. Colors represent regions in Fig. 4B

Table 3 The shape model of Helene.

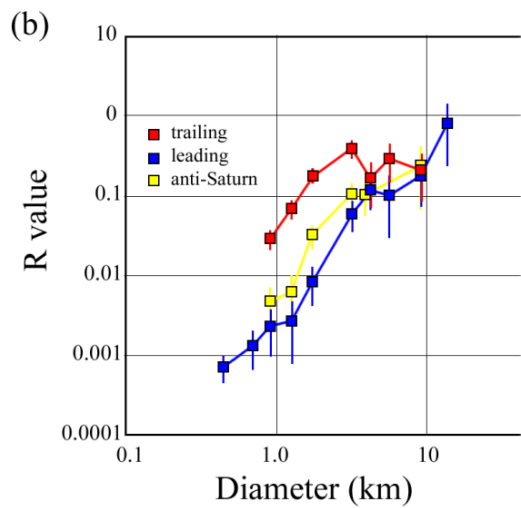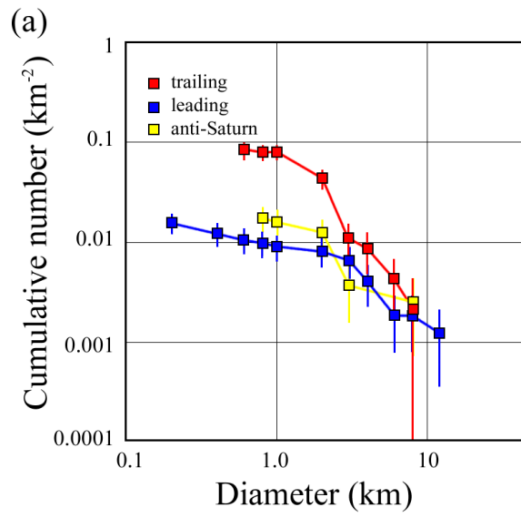|	-90	-80	-70	-60	-50	-40	-30	-20	-10	0
10	15719	16069	17066	17412	17580	17316	17762	18518	18627	19301
20	15719	16118	17164	17965	17136	16887	16965	17477	17615	19290
30	15719	16788	17667	17833	16614	15878	16488	17165	17942	19555
40	15719	16832	18213	17387	16331	15584	16611	17680	18183	19842
50	15719	17436	18514	18063	16891	16483	17713	19066	19259	20455
60	15719	17083	18489	18551	17935	17599	19735	20206	21084	21303
70	15719	16629	18600	19465	18868	19917	21033	21439	21834	21483
80	15719	16860	18305	19950	20168	20823	20662	20580	21029	21519
90	15719	16642	18014	19834	20371	19991	19891	19973	20445	20190
100	15719	17323	17578	19500	20204	19788	19120	19000	19083	19171
110	15719	16775	17773	18689	19949	19526	18859	18368	18413	18304
120	15719	16493	17154	18547	19206	19136	18405	17958	17485	17800
130	15719	16950	17247	19127	18399	18584	17652	17296	17209	17786
140	15719	16684	17029	18054	17497	16505	16472	17584	17829	18238
150	15719	16422	17193	17202	15845	15814	16503	17854	18791	18907
160	15719	16620	17375	16870	15976	16579	17272	18618	19780	19309
170	15719	16422	16842	17088	16409	17156	18150	19477	19448	19366
180	15719	16471	16842	16941	17107	17454	17799	18700	18445	18991
190	15719	16169	16379	16599	15755	15712	16400	17789	18065	18734
200	15719	15829	16120	16469	15041	14804	16174	17994	18074	18438
210	15719	15892	15939	16302	14986	14933	16598	17877	18345	19109
220	15719	15463	15705	16039	15444	16170	16367	17738	17904	19962
230	15719	15426	15421	15729	15655	15901	16347	17168	18645	19985
240	15719	15245	15316	15385	15476	15630	16243	18403	19761	20758
250	15719	15033	15019	15713	15213	15810	17398	19787	20155	19799
260	15719	14827	15143	15834	15317	15910	17476	18864	19565	19366
270	15719	14721	14828	15979	15638	15834	16764	18138	19620	19654
280	15719	14721	14764	16167	16272	16289	17253	17600	19152	20311
290	15719	15081	14699	16137	17002	17549	18013	18626	19235	20560
300	15719	14751	15010	15727	17884	18929	18927	19303	19840	20999
310	15719	14631	14698	15496	16788	19341	21007	20913	21313	23335
320	15719	14689	14624	15242	16385	19013	21797	23464	22170	23716
330	15719	14990	15116	15254	16356	18645	21024	22527	22825	24493
340	15719	15095	15299	16394	17989	18658	20591	22377	23696	24295
350	15719	15495	16033	17199	18424	18873	19090	20513	22235	23889
360	15719	15448	16041	17513	18104	17938	18441	19771	20585	21219

* The distance (in meter) between the geometric center and the surface based on the shape model of Helene (latitudes in horizontal lines and longitudes in vertical lines)

Part 1

Table 3 Continued

	10	20	30	40	50	60	70	80	90
10	21110	21699	20990	21250	17418	15180	14501	14501	14123
20	19741	20372	21452	20763	18191	14735	14735	14287	14123
30	19724	20289	21407	20435	17267	15683	14287	13796	14123
40	20360	20946	20984	20420	18149	15075	15075	13796	14123
50	20839	21721	21270	19618	17323	15790	14996	14996	14123
60	21115	20943	19210	18956	17693	16577	14996	14415	14123
70	21676	21636	19871	18491	18358	15799	15257	14415	14123
80	21169	20968	20128	18906	18127	16118	15257	14874	14123
90	20488	20593	20619	19961	18550	17017	14874	14874	14123
100	19355	19766	19965	19896	18960	17602	15093	14395	14123
110	18664	18971	19565	19568	18650	16792	15093	14395	14123
120	18336	18792	19290	19966	18449	16860	15425	15425	14123
130	18842	18882	19463	19914	18576	17229	14680	14680	14123
140	18975	19689	19493	19744	18066	16745	15382	14680	14123
150	19892	20587	20282	19704	18495	15688	15688	14085	14123
160	19437	20404	20255	20236	18057	15872	14906	14085	14123
170	19885	19626	19090	19412	18021	16207	14906	14085	14123
180	18384	18796	18067	18318	17847	15978	15370	14443	14123
190	18416	18646	19504	19225	17566	15339	14443	14443	14123
200	18809	18173	18182	18656	17500	15912	14443	14443	14123
210	20217	18599	18611	18428	16851	15108	15108	13802	14123
220	19348	18668	19876	17972	16686	15618	14365	13802	14123
230	18947	18183	19082	17919	16843	15618	14365	13802	14123
240	18796	18120	17904	17510	16841	14891	14891	13802	14123
250	19151	18110	18039	18296	15774	15774	14141	14141	14123
260	19405	18434	19003	18438	16835	14970	14141	14141	14123
270	20183	19375	20207	19341	16546	14970	14970	14141	14123
280	21280	21238	21525	20015	16663	15683	14633	13796	14123
290	21432	21322	21044	19289	17001	14633	14633	13796	14123
300	22323	21829	21497	18880	16428	15365	13796	13796	14123
310	24042	23414	21414	18364	16768	15365	14376	13796	14123
320	24860	24022	23296	19191	15850	14376	14376	14376	14123
330	25153	26533	24608	19913	17419	15850	14376	13888	14123
340	25363	25322	24404	20236	16073	14820	13888	13888	14123
350	23330	22643	21239	21370	17362	14820	13888	13888	14123
360	22822	21701	20832	20573	18902	15577	14501	13888	14123
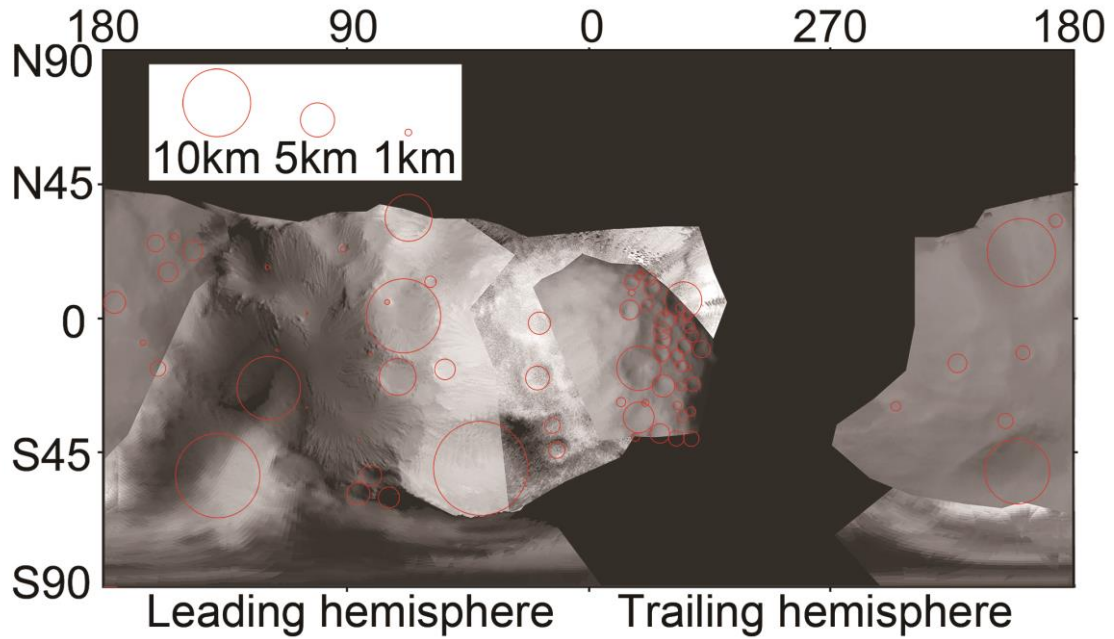
Figure 6 The distribution of craters on Helene.

The distribution of craters (red circles) on Helene on a cylindrically-projected global image created from images listed in Table 2. Black region lacks images (craters cannot be identified in this region). Note that I identified craters in raw images rather than this projected image. Some craters on the anti-Saturn side of the trailing hemisphere (longitude 180-270°) might remain unidentified due to low solar incident angles of the images.

3. Surface feature on Helene

3.1. Streaky depressions

One of the notable features found on Helene is a linearly curved gully-like depression (hereafter streaky depressions) (Fig. 2A-C). Their depths are difficult to measure, but are probably a few tens of meters from the shadow measurement. Streaky depressions commonly exist on a slope as a group with sharing their directions. As for the case of craters, the distribution of streaky depressions varies significantly from place to place; For example, numerous streaky depressions found on slopes of a basin of the leading hemisphere (Fig. 2A), while no such depressions are found on the trailing hemisphere (Fig. 2D). Importantly, I find that a terrain with streaky depressions has a small number of craters, while a terrain covered by numerous small craters has no streaky depressions. In other words, all streaky depressions only exist in the less cratered terrain shown in Fig. 4B.

I critically compare the local gravity and the direction of streaky depressions. As a result, I find (1) all streaky depressions strictly follow the local gravity (Fig. 7); (2) A streaky depression exists only on a slope but not on a flat terrain; (3) The minimum slope-angle for the existence of a streaky depression is about 7 degree. These findings indicate that the streaky depression are results of (or associated with) some kind of mass movement processes. This may explain the fact that the general appearance of a streaky depression is similar to terrestrial gullies formed on powdery snow deposits or sand dunes.

Terrestrial gullies sometimes show structures--such as alcoves (funnelform depressions extending from the top of the slope), channels (linear depressions extending from the narrow stem of an alcove), and fans (cone-shaped deposits crossed by streams)--that indicate transport of material from the top to bottom of the slopes (McClung and Schaerer 1993). Analogously to such terrestrial gullies, streaky depressions on Helene sometimes exhibit alcoves and channels (Fig. 2C), further supporting the idea that streaky depressions are formed by gravity-induced mass movements.

Perhaps, the deficiency of fans may be due to the tiny gravity, which can make the particles be easily to spread.

3.2. Unusual smoothness of the leading hemisphere of Helene

The unusual smoothness of the leading hemisphere is evidenced by the lack of shadows, even at the areas with large illumination angles. The smoothness likely indicates that the surface of Helene is covered by small particles. Unlike craters in heavily cratered terrain, the shapes of large craters on the leading hemisphere are not quite simple; their inner shapes are not parabolic but somehow flattened. Also, almost no small craters can be identified on the leading hemisphere.

These may indicate that fine particles has deposited and modified or erased craters only on the leading hemisphere. This idea might also be supported by the fact that streaky depressions, presumably resulted from mass-movement of fine particles on the surface, only exist on the leading hemisphere.

3.3. Origin of the fine particles on the leading hemisphere

I consider that these fine particles come from the E-ring because (1) Helene exists in the orbit of the E-ring, which may indicate that material from the E-ring continuously fall into Helene; (2) The visual and infrared spectra of Helene are known to be similar to that of the E-ring (Filacchione et al. 2010); and (3) The leading hemisphere appears to be abundant in small particles than other regions, which is most easily explained by accumulation of the E-ring material on Helene. In fact, Hamilton and Burns (1994) shows that accumulation of the E-ring material occurs mostly on the leading hemisphere, because an angular velocity of a particle of the E-ring is slower than that of Helene when the particle reaches around Helene after its emission from Enceladus. Dione, which is the co-orbital satellites with Helene, is known to have an albedo dichotomy (the leading hemisphere is 1.8 times brighter than the trailing hemisphere) (Verbiscer et al. 2007), which is considered as a result of accumulation of the E-ring material to Dione's leading hemisphere (Buratti and Veverka 1984, Jaumann et al. 2009). As a result, particles supplied from the E-ring can be considered to cause the appearance of the leading hemisphere of Helene as I mentioned

above.

3.4. Thickness of the E-ring material on Helene

      Shadows of streaky depressions indicate that the thickness of the E-ring material are typically a few tens of meters, which implies that the E-ring deposits in which the depressions form must be at least ten meters thick. Moreover, the leading hemisphere shows the near-absence of small craters (less than ~3 km across; Fig. 5). This indicates that the deposits are unlikely to be more than a few hundred meters thick. Therefore, I estimate that the thickness of the deposits on Helene accumulated from the E-ring is between 10 and 300 m.
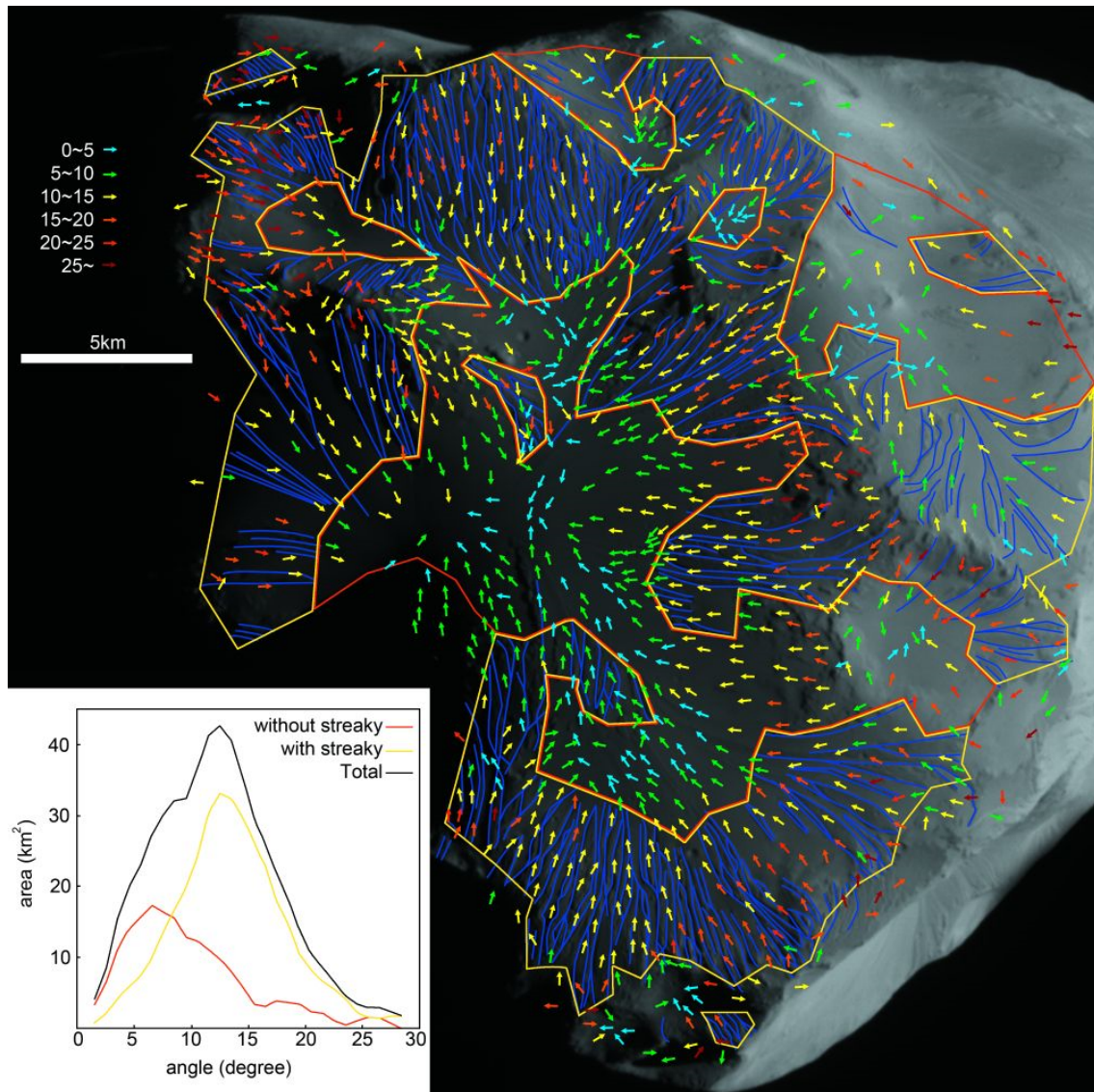
Figure 7a Surface gravity on Helene.

The leading hemisphere of Helene (N1687120437) with arrows indicating the directions of the local gravity (color represents slopes). Blue lines indicate streaky depressions. The regions enclosed by yellow or red lines are the regions with and without streaky depressions, respectively. Streaky depressions exist on steeper (> ~7 degree) and strictly follow the directions of surface gravity. Inset shows the total areas of both regions as a function of slope angle, whose values are shown in Table 4.
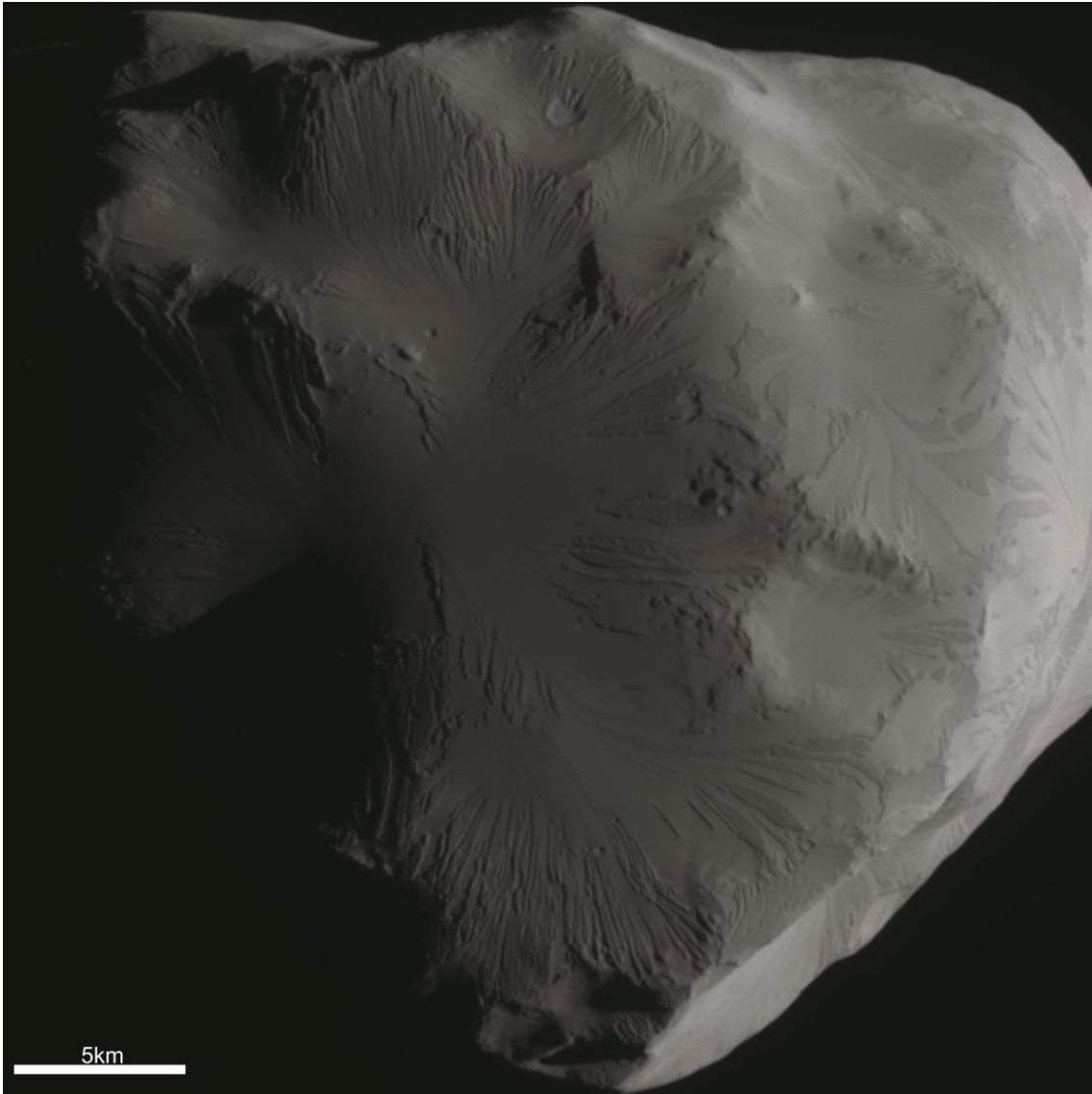
Figure 7b Surface gravity on Helene.

The Leading hemisphere of Helene (N1687120437). This image is used for the background of Figure 7a.

Part 1

Table 4 Angles of slopes to areas

Angle	Area with streaky depressions (km^2)	Area without streaky depressions (km^2)	Total (km^2)
0 ~ 1	0.00	2.23	2.23
1 ~ 2	0.70	2.88	3.58
2 ~ 3	1.54	4.81	6.35
3 ~ 4	3.86	11.62	15.48
4 ~ 5	7.04	16.75	23.79
5 ~ 6	6.65	13.18	19.83
6 ~ 7	8.48	16.88	25.36
7 ~ 8	14.75	21.54	36.30
8 ~ 9	17.52	10.81	28.33
9 ~ 10	17.58	14.17	31.75
10 ~ 11	23.97	13.37	37.34
11 ~ 12	31.08	9.52	40.60
12 ~ 13	35.80	10.27	46.08
13 ~ 14	32.15	9.22	41.36
14 ~ 15	29.45	4.93	34.38
15 ~ 16	27.17	2.86	30.04
16 ~ 17	21.58	2.34	23.92
17 ~ 18	19.83	3.88	23.72
18 ~ 19	12.43	5.35	17.78
19 ~ 20	11.34	1.18	12.53
20 ~ 21	7.18	3.59	10.78
21 ~ 22	6.09	1.96	8.05
22 ~ 23	6.36	0.57	6.93
23 ~ 24	3.87	0.49	4.36
24 ~ 25	2.31	0.00	2.31
25 ~ 26	0.55	2.67	3.22
26 ~ 27	1.44	1.83	3.27
27 ~ 28	2.05	0.00	2.05
28 ~ 29	1.63	0.00	1.63
> 29	1.07	0.00	1.07

4. Accumulation of E-ring material on other satellites

I show the surface of Helene is strongly influenced by the E-ring material. This might be true for other satellites in the E-ring region, especially, Calypso, Telesto, Pallene, and Methone because of higher densities of the E-ring near the orbits of these satellites (Fig. 8).

4.1. Telesto and Calypso

Telesto and Calypso have unusually smooth surfaces similar to each other (Fig. 2E, F). In fact, craters on Telesto and Calypso generally exhibit softened blanketed morphologies with indistinct rims (and sometimes such craters are almost entirely erased), similar to craters on the leading hemisphere of Helene. Large (>5 km diameter) craters on Telesto and Calypso appear to be buried just as small craters are on Helene. Also, Calypso exhibits streaky depressions (Fig. 2E), which are similar to those on Helene. I examine the crater size-frequency distribution on the leading hemisphere of Telesto (Fig. 9), which is consistent with that on the leading hemisphere of Helene. Spectral observations demonstrate the contribution of the E-ring material on their surfaces (Buratti et al. 2010), which supports the view that, as with Helene, the E-ring material accumulated on these satellites into thick deposits.

4.1.1. The depth of the E-ring material on Telesto and Calypso

Despite the above similarities, Telesto and Calypso are different from Helene in several aspects. For example, these satellites accumulate the E-ring material more than Helene. In fact, Telesto and Calypso almost completely lack large craters (>5 km diameter). Moreover, the few existing craters are almost entirely erased. Furthermore, the global shapes of Telesto and Calypso are closer to a smooth ellipsoid. This fact suggests that the depth of the E-ring deposits on Telesto and Calypso are at least several hundred meters, which is roughly twice as deep as those on Helene. This difference may be due to the densities of the E-ring. The E-ring is known to be denser closer to Enceladus (Verbiscer et al. 2007).

Therefore, the E-ring at the orbit of Telesto/Calypso exhibits higher brightness than at the orbit of Helene, which may explain the thicker deposits on Telesto/Calypso relative to those on Helene.

4.1.2. Lack of hemispheric dichotomy for Telesto or Calypso

Unlike Helene, Telesto and Calypso appear to have smooth surfaces and few small craters even on their trailing hemispheres (though Calypso's trailing hemisphere has yet to be observed at high resolution), which suggests that Telesto and Calypso lack any dichotomy (Fig. 10). This diversity may be explained by the motion of the E-ring particles.

The dynamics of the E-ring particles is difficult to directly observe and can be surprisingly complex due to the competing effects of the gravity of satellites, solar radiation pressure, electrostatic grain potential, the Lorenz forces, the plasma-sputtering, and plasma drag (Horányi et al. 2009, Horányi et al. 2008). Nevertheless, these forces cause large orbital eccentricities or an increasing of semi-major axes, which result in correspondingly large radial excursions of E-ring particles in just a few years (Horányi et al. 2009, Horányi et al. 1992). Especially, large orbital eccentricities of E-ring particles having the semi-major axis close to Enceladus can play an important role in the hemispheric dichotomies on satellites.

Within the orbit of Enceladus, E-ring particles move faster than satellites. This causes E-ring particles to collide preferentially onto the trailing side of Mimas. On the other hand, beyond the orbit of Enceladus, E-ring particles move slower and are overtaken by satellites, which causes E-ring particles to collide preferentially onto the leading sides of Dione and Tethys. This can also explain Helene's hemispheric dichotomy. I note that average angular velocity of an E-ring particle relative to an encountered satellite depends on distance from Saturn. This would naturally cause the impact distribution of particles onto the satellite surface to vary with distance from Saturn. Because Tethys is closer to Enceladus than Dione, the average velocity of E-ring particles in the orbit of Tethys is less decelerated compared with that in the orbit of Dione. Therefore, interactions with particles might not be concentrated

significantly on the leading hemisphere of Tethys, Telesto, and Calypso. In fact, this view is consistent with both the small but not negligible albedo difference (1.1 times) between the leading and trailing hemispheres of Tethys and enhanced albedo difference (1.8 times) of Helene.

The lack of a hemispheric dichotomy on Telesto and Calypso may be due to not only E-ring particle dynamics but also to possible non-synchronous rotation of these satellites. Non-synchronous rotation re-orients the satellite, causing the leading and trailing hemispheres to migrate across the satellite figure and preventing preferential particle deposition on any specific hemisphere of the satellite.

4.2. Pallene and Methone

Pallene (Fig. 2G) has a featureless smooth spherical shape, which is unusual for a body of only ~2.2 km in radius. Methone (Fig. 2H) also shows an unusual smooth surface without undulation. Methone is likely quite similar to Pallene in terms of size, shape, and smooth appearance (e.g. Thomas et al. 2013). I note that such characteristics are quite unusual for small satellites or bodies including asteroids. The mean radii of Pallene and Methone indicate that their gravities are not large enough to maintain their spherical shapes.

Spherical shapes of Pallene and Methone (perhaps also Anthe, the other of the Alkyonides) are also possibly related to the E-ring. Interestingly, the density of the E-ring material around Pallene is also large (denser than Tethys) and its orbit is near Enceladus. Therefore, I consider that the E-ring material also accumulates on Pallene or Methone globally to bury original irregular shape of the satellites resulting in forming its current spherical shape. Otherwise, it might be complicated by the existence of the co-orbital ring and the arc coexisting with both Pallene and Methone, whose materials might originate from these satellites (Hedman et al. 2009).

In any case, both of these tiny satellites are difficult to immediately accumulate material released by impacts, which may temporary form the ring or arcs. Nevertheless, these released

materials, originally from both the E-ring and satellites, should re-accumulate on the satellites because of the confinement of dust in resonances with Mimas or Enceladus. These processes may explain their unusual smooth surfaces and spherical shapes. I suspect that Anthe also has a spherical shape with a smooth surface.

4.3. Mid-sized satellites

Unlike the small satellites, the E-ring deposits on Tethys and Dione are probably quite thin because (1) these satellites' radar-optical albedo appear to decrease with distance from Enceladus (Ostro et al. 2010); (2) crater statistics (Kirchoff and Schenk 2010) indicate no deficiency of craters on either Tethys or Dione, in contrast to Helene and Telesto; and (3) high-resolution images of Tethys and Dione show no unambiguous evidence for thick deposits, such as streaky depressions. Nevertheless, albedo (Verbiscer et al. 2007), spectral (Filacchione et al. 2010), and thermal inertia (Howett et al. 2010) measurements indicate thin but non-zero deposits of E-ring particles on these mid-size satellites. Thus, E-ring particles are likely deposited widely on Tethys and Dione, but the resulting deposits are much thinner than those on the small satellites. Possible explanations are differences in the dynamics of E-ring particles among the satellites or higher impact velocity onto the mid-sized satellites, however, the reasons for this difference are unknown.
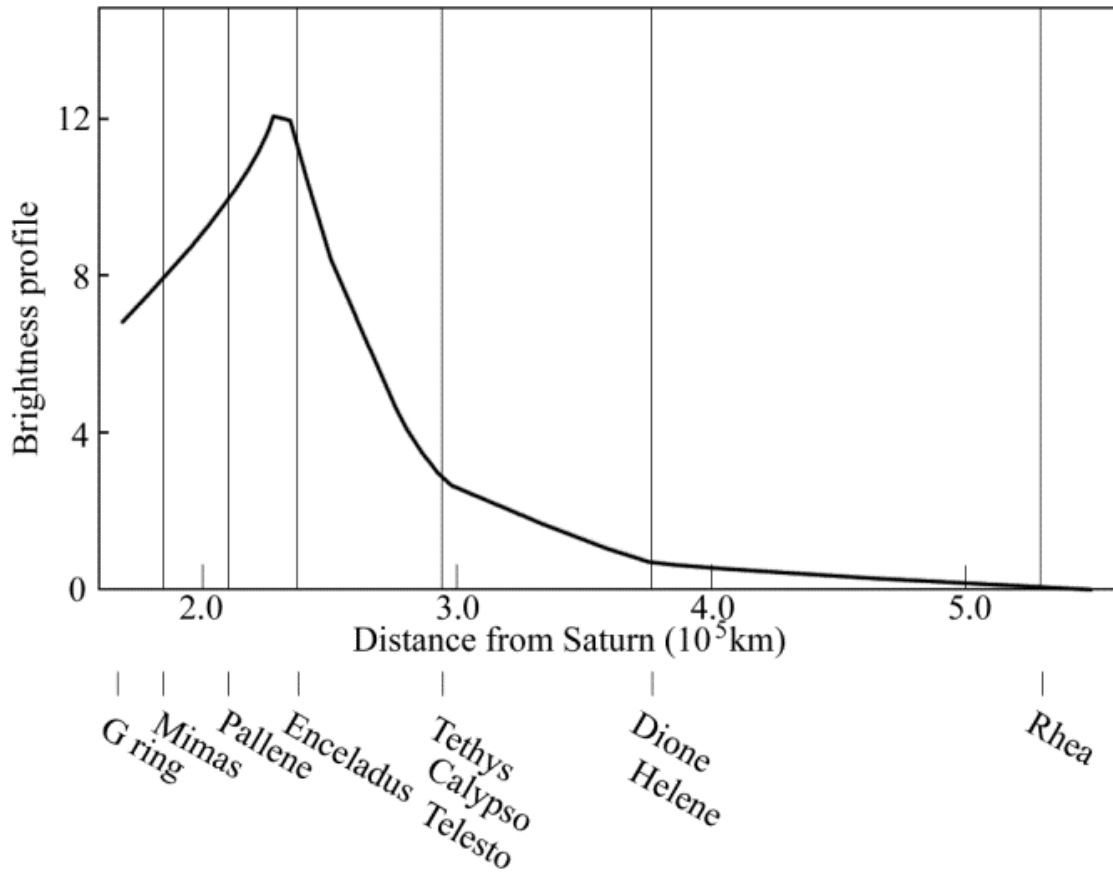
Figure 8 Brightness profile of the E-ring.
Brightness profile of the E-ring as a function of radial distance from Saturn based on (Baum et al. 1981). Brighter value means the E-ring being denser. As shown in this image, brightness in the orbit of Enceladus is the highest and that of Tethys, Telesto, and Calypso are higher than that of Helene.
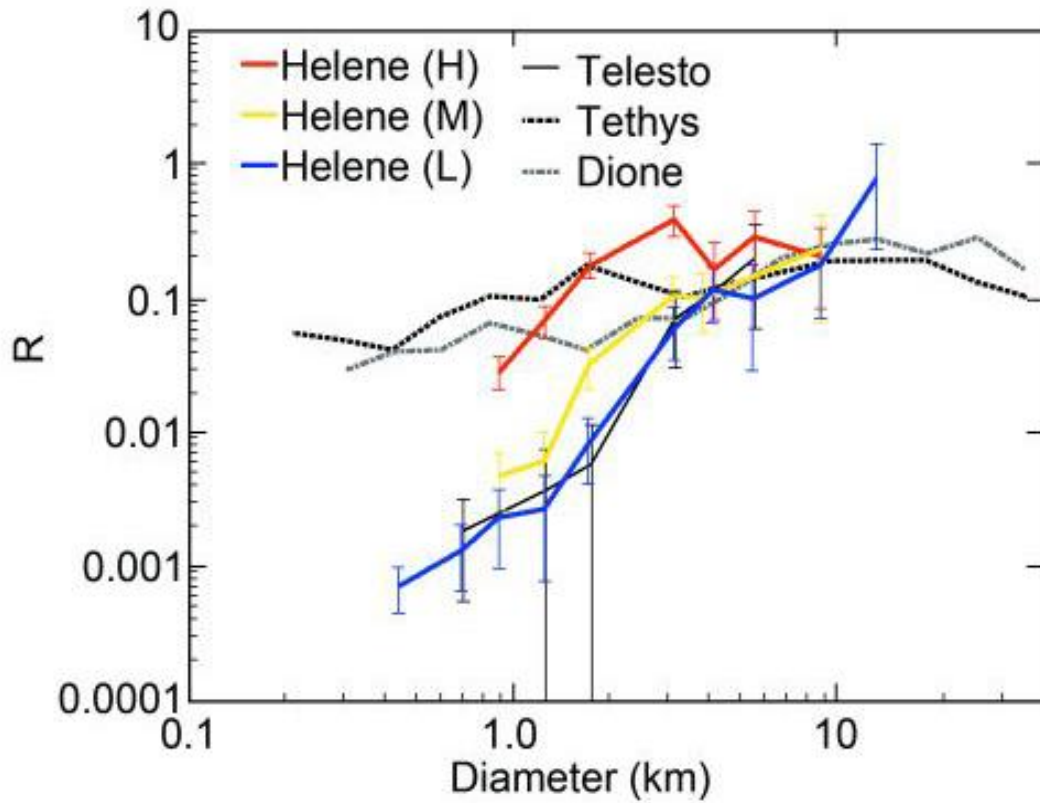
Figure 9 Relative size-frequency distributions of craters.
Relative size-frequency distributions of craters of heavily cratered terrain (H), moderately cratered terrain (M), and less cratered terrain (L) of Helene as well as the trailing hemisphere of Telesto (Telesto), heavily cratered terrain on Tethys (Tethys), and heavily cratered terrain on Dione (Dione). The data for Tethys and Dione come from Kirchoff and Schenk (2010).

Figure 8 Telesto and Calypso.
Telesto (upper) and Calypso (lower) at the same scale, showing smooth surfaces in both leading and trailing hemispheres (upper left N1514163666, upper right N1630076968, lower left N1506184171, lower right N1644754662).

5. Implications to the age of the cryovolcanism of Enceladus

5.1. The age of the E-ring deposits

I estimate the age of the E-ring deposits based on the cratering rate. The high crater density on the trailing hemisphere of Helene indic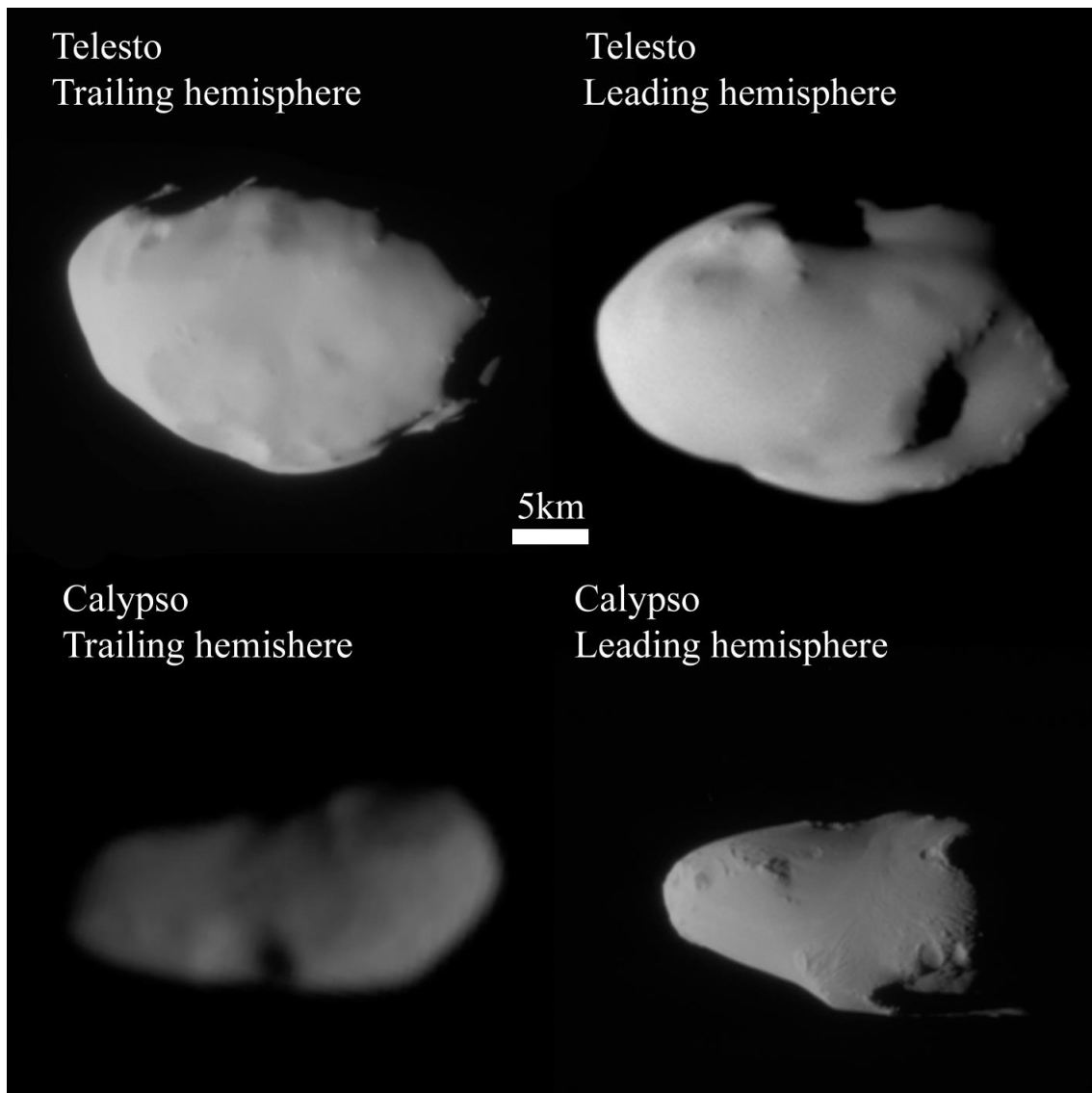ates that Helene is basically an old satellite. Based on the crater chronology of the saturnian system (Zahnle et al. 2003), I estimate that the age of the heavily cratered terrain is ~4.0 Gy (and at least ~1.0 Gy), which coincides with the age estimated from the distribution of large craters (>5 km). I also find that the distribution of craters exceeding 5 km in diameter on Helene and Telesto are generally similar to those of Dione and Tethys (Fig. 9), which indicates that, in general, the original crater densities of small satellites are similar for these mid-sized satellites.

On Helene's E-ring deposit, whose area is 1,637 km^2, I identify 5 craters of ~200 m in diameter but not exceeding 1 km. This clearly indicates the deposits are young, but estimating the age can be more complicated than the Moon. This is mostly due to the lack of dated samples from the saturnian satellites and to the difficulty in determining the cratering rate, which should be estimated theoretically based on the populations and orbits of potential impactors. According to Dones et al. (2009), potential impactors come from (i) main-belt asteroids, (ii) trojan objects of the gas giants, (iii) Centaurs and ecliptic comets, (iv) Saturn's irregular satellites, (v) planetocentric bodies, and (vi) Nearly Isotropic Comets. Especially, Zahnle et al. (2003) estimates that primary impactors on saturnian satellites are trans-Saturnian objects such as Centaurs.

Therefore, the theoretical study for cratering rate (Zahnle et al. 2003) is based either on (A) the crater densities on the Moon, Europa, Ganymede, and Triton, and (B) the statistics of encounter with potential impactors. Their populations and orbital properties (Gladman et al. 2001) are studied with ground-based observations, even though the accurate size-frequency of small objects is still

unknown because of their great distances. Zahnle et al. (2003) estimates the cratering rate for the outer Solar System, including that on saturnian small satellites; for example, the cratering rate (D > 1 km) on Helene is (A) 2.0×10^{-7} craters per 10^3 km^2 per year if I assume that small objects obey a nearly collisional distribution and (B) 2.0×10^{-9} craters per 10^3 km^2 per year if I assume the size–number distribution is like that inferred at Jupiter. Therefore, assuming this cratering rate, the age of the E-ring deposits on Helene is likely to be 0.3-5 My (the former case) or 200-500 My (the latter case).

On the other hand, according to Dones et al. (2009) if major potential impactors originated from heliocentric objects, such as Centaurs, impact cratering on saturnian satellites should exhibit a hemispheric dichotomy because heliocentric impactors strongly favor cratering of the leading hemisphere. However, small craters on saturnian satellites do not show such dichotomies, which may imply that planetocentric impactors, such as secondary or sesquinary impactors, are dominant to form smaller craters. If I assume that the heavily cratered regions on Helene, which have 100 craters larger than 1km in diameter per 10^3 km^2, was formed more than 4 Gy and that the cratering rate is constant for its life time, I obtain ~40 My for the age of the E-ring deposit on Helene. Or, if I assume the crater distribution on Dione (Kirchoff and Schenk 2010), whose Trojan satellites include Helene, indicate that the crater formation rates of > 1km craters is 7.5×10^{-6} craters per 10^3 km^2 per year and of > 200 m craters is ~10^{-7} craters per 10^3 km^2 per year, I obtain ~50 My for the age of the E-ring deposit on Helene.

I note that these estimates include ambiguities in their assumptions. However, importantly, all these independent estimates coincide around several ten My. Thus, I conclude several tens of million years or younger for the most likely ages of the E-ring deposit on Helene.

5.2. The cryovolcanism of Enceladus

The E-ring deposit on Helene is fairly thin, as thick as a few ten or hundred meters, while the depth of a crater is relatively deep enough (a crater with a few hundred meters in diameter should

have a few ten meters in depth). In other words, the E-ring depositions are difficult to bury newly-formed craters (larger than ~1 km in diameter) after initiation of the deposition. In addition, Helene and Telesto, which partly appear the heavily cratered surface, must be significantly older than that of the E-ring. Thus, I consider that the deposits on Helene are suitable to discuss when the Enceladus' cryovolcanism has begun. If so, the accumulation of the E-ring material has begun at most 100 My ago as a result of initiation of cryovolcanism on the surface of Enceladus. Interestingly, the age of the E-ring deposits on Helene is consistent with the previous estimate of the endogenic activity in Enceladus I mentioned in section 1.

Otherwise, the E-ring deposits may be occasionally eroded by a large impact. Such a large impact may potentially remove a large amount of surface material from Helene because of Helene's tiny gravity. In addition, small satellites, such as Helene, may be ephemeral because the orbits of the small satellites are not as stable as those of mid-sized satellites. If so, the age of the E-ring deposits may be older than I estimated above. I think the issues may be subjects of future investigations.

Part 2

This part shows my previous study which discussed the geological features on Atlas, a small inner satellite of Saturn. In summary, I found the interaction between the main ring and Atlas, which form the unusual surface of Atlas. This content has been published in Hirata and Miyamoto (2012).

Atlas has an enigmatic saucer-like shape explained by an accumulation of particles from A-ring of Saturn. However, its unusual smooth surface remains unexplained. Gardening through continuous particle impact events cannot be a unique explanation for the smoothness, because Prometheus does not exhibit a similar surface, though it too would have experienced a similar bombardment. Here, a detailed investigation using close-up images of Atlas reveals the surface to be (1) covered by fine particles (i.e., probably as small as several tens of micrometers); (2) mostly void of impact craters (i.e., only one has been thus far identified); and (3) continuously smooth, even between the equatorial ridge and the undulating polar region. These findings imply that some sort of crater-erasing process has been active on the surface of Atlas. From electro-static analyses, I propose that the upper-most layer of the fine particles can become electro-statically unstable and migrate as a result of dust levitation, which resulted in erasing craters on the surface of Atlas. If true, Atlas would represent the first recognized body where resurfacing is dominated by dust levitation.

1. Small satellites of A-ring

Saturnian inner satellites coexist with surrounding ring in the same orbit, which indicates interaction between satellites and ring materials should occur. Saturn has the most massive, diverse and extensive ring system in the solar system. Saturnian rings are divided into D, C, B, A, F, G, and E-ring from within outward, depending on their properties and regions. Especially, A, B, and C rings are known as the main ring. The locations and characteristics of these satellites are shown in Fig. 11 and Table 5, respectively.

Pan, Daphnis, and Atlas are located at Encke gap, Keeler gap, and outer edge of A-ring, respectively (Fig. 12). Atlas was discovered in 1980 from images taken by Voyager 1 (Smith et al. 1981). After that, Pan was discovered in 1990 from reanalysis of images taken by Voyager 2 (Showalter 1991). Following them, Daphnis was discovered in 2005 from images taken by Cassini (Porco et al. 2005). Prometheus and Pandora, located at inner and outer edge of F-ring, respectively (Fig. 13), are discovered in 1980 during Voyager 1 flyby (Smith et al. 1981). These satellites are also known to be shepherd satellites whose gravities serve to maintain sharp edges of rings or gaps. These satellites are the innermost satellites of Saturn system, which mean the much strong tidal force acts on these satellites.

The shapes of small satellites in the A-ring region are close to a disk, with equatorial radii of 16.5 and ~19.5 km, and polar radii of ~10.5 km and 9 km for Pan and Atlas, respectively (Charnoz et al. 2007). Both Atlas and Pan have a prominent equatorial ridge, which is roughly symmetric around the equator of the body, resulting in their overall shapes being close to a disk (Daphnis may also have the same nature). In contrast to Atlas's or Pan's symmetric shape, the shapes of Prometheus and Pandora are simply close to oblate distorted ellipsoid. Except for a small asteroid, 1999KW4, no other solar bodies are known to have similar shapes of Pan or Atlas (Minton 2008). The disk-like shape of 1999KW4 is likely related to the strong centrifugal force caused by its fast rotation speed (e.g. Walsh et al. 2008). However, this effect cannot explain the shapes of

Atlas or Pan because their rotation periods T (~14hours) are too slow to form their equatorial ridges (Charnoz et al. 2007). On the other hand, tidal force is also inadequate to explain their shapes because the saturnian tidal stress simply elongates the satellites in the radial direction rather than creating an equatorial ridge (Charnoz et al. 2007). Charnoz et al. (2007) propose that the equatorial ridges of Atlas and Pan are kilometer-thick piles of ring-particles, whose orbital distributions have been flattened enough to accrete into equatorial ridges. Thus, the accretions of the ridges occur after the flattening of the rings but before complete depletion of ring material from the surroundings, such as A-ring. In fact, the spectra of these satellites obtained by Cassini are quite similar to that of A-ring (Filacchione et al. 2010, Buratti et al. 2010) and these satellites have low densities, as low as half of ice (Porco et al. 2007) (Table 5), which is considered to indicate rubble pile structures consisting of icy ring particles, supporting the idea of growth of the satellite by accretion.

Ring materials of A-ring or F-ring cannot accrete onto these satellites under their self-gravity at the present time because their surfaces spread out of their Roche lobe. Roche lobe is the gravitational equipotential surface which contains L1 point. If the surface materials are fluid and expand Roche lobe, then the surface materials escape to the planet through L1 point. The volume of a satellite relative to that of Roche lobe simply depends on its density and distance from the planet. This density can be described as the critical density. Ring particles of A-ring or F-ring are also lower than this critical density, which means ring materials cannot also accrete under their self-gravity.

Furthermore, the observed densities of satellites of A-ring and F-ring regions are close to the critical densities of these satellites, which mean that these satellites entirely fill their Roche lobe and ring materials can no longer accrete onto their surface (Porco et al. 2007) (Table 5). The observed spectra and satellites' shapes indicate these satellites have formed by accretions of A-ring materials, however, A-ring particles cannot also form satellites as I mentioned above. This indicates the existence of high density

buried core (or cores) at the centers of satellites (Fig. 14). Thus, high density embryos should have initially existed before these satellites have formed (Charnoz et al. 2007). In fact, the polar region of Atlas is characterized by both similarly-sized (a few km-scale) mounds and depressions, which might reflect the internal structure of Atlas. Porco et al. (2007) also proposed that similarly-sized buried cores exist at the center of Atlas.

　　　The high resolution images of Atlas show that Atlas has unusual smooth surface (Fig. 15). Note that surface features of Pan or Daphnis are unfortunately unknown. For example, no crater has been found on the surface of Atlas (Charnoz et al. 2007), which is surprising because the A-ring contains numerous large particles (up to a few km size), and some should have impacted on Atlas during accretion. In addition, a lot of impact craters should be also formed after Atlas's formation in the same way as other Saturn's satellites.
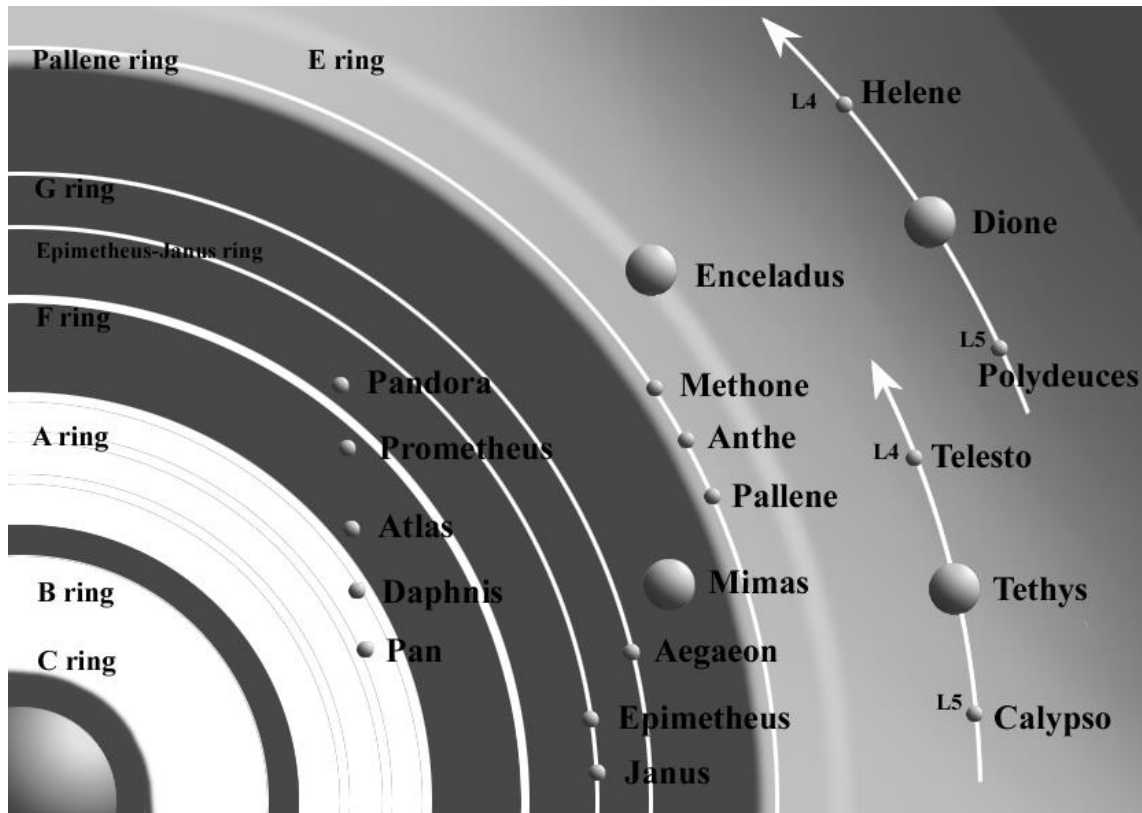
Figure 9 The locations of saturnian small satellites.

Table 5 Inner small satellites.

	Semi major axis (km)	Mean radius (km)	Mass ($\times 10^{19}$g)	Density (g/cm^3)	Porosity (%)	Roche lobe (%)
Pan	133584	14.2±1.3	0.495	0.41±0.15	54	109
Daphnis	136504	3.9±0.8	0.0084	0.34±0.21	62	125
Atlas	137670	15.1±1.4	0.66	0.46±0.10	49	89
Prometheus	139380	43.1±2.7	15.67	0.47±0.065	48	85
Pandora	141720	40.3±2.2	13.56	0.50±0.085	44	76
Janus	151460	89.6±2.0	188.91	0.63±0.063	30	49
Epimetheus	151410	56.7±1.9	53.07	0.69±0.13	23	44

*1 The ratio of the Volumes of satellites out of Roche lobe
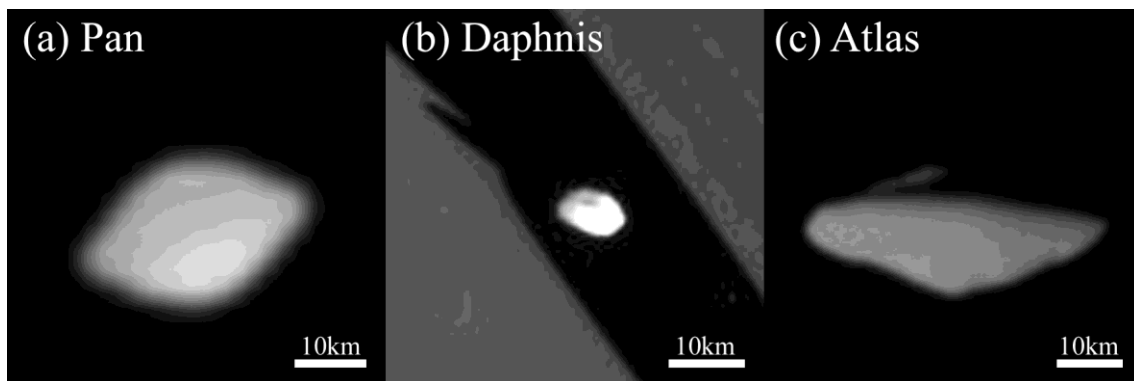
Figure 10 Satellites of A-ring region.
(a) Pan (~3km/pixel) (PIA08405), (b) Daphnis (N00156643), (c) The trailing hemisphere of Atlas (~1km/pixel) (PIA08405).
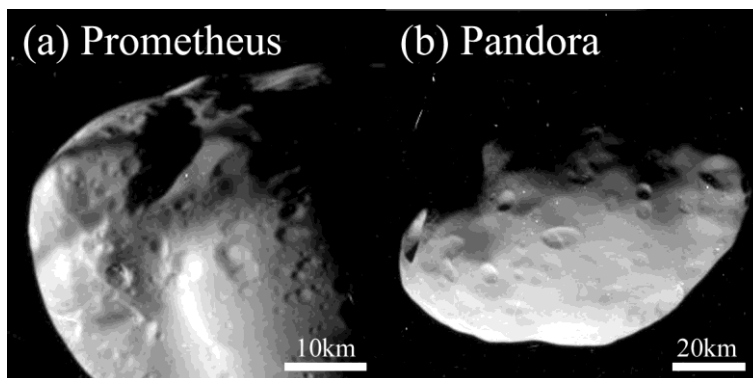
Figure 11 Satellites of F-ring region.
(a) Prometheus (N00150211) and (b) Pandora (N00039262). The high resolution images of Prometheus and Pandora show these satellites have numerous craters, in contrast to the case of Atlas. In detail, Prometheus has more numerous small craters than Pandora.
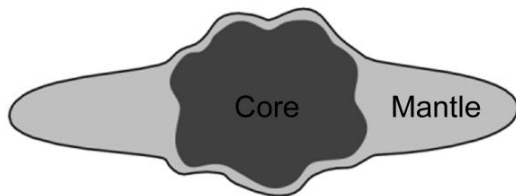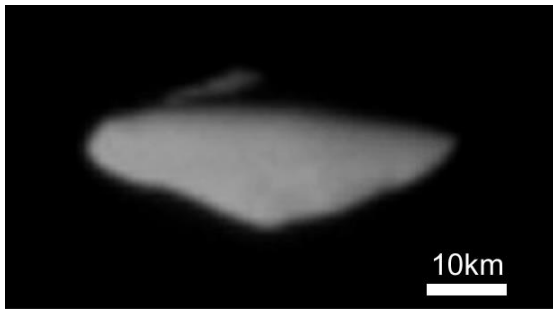
Figure 12 Hypothesized cross-section of Pan and Atlas.
The similarly-sized mounds and depressions at the polar region may be explained by the existence of a bumpy core (or similarly-sized cores). Smoothness of the bumpy polar region indicates the existence of a thin layer that consists of the same materials as the equatorial parts of Atlas.
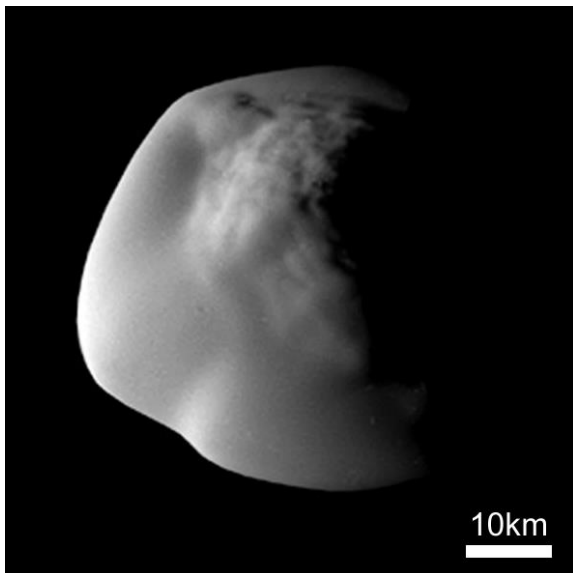
Figure 13 The highest-resolution image of Atlas.
This image shows its southern hemisphere at the resolution of ~320m/pixel (PIA08405).

2. Geological study of Atlas

As discussed above, previous works (Porco et al. 2007, Charnoz et al. 2007) only revealed its shape and low density with discussions regarding its formational process. However, the unusual smoothness of the surface of Atlas remained unexplained. I find the smoothness holds important key in understanding the evolutionary history of Atlas, Pan, and some other small satellites of Saturn. In the following, I describe my new geological observations of Atlas and propose a new theory to explain my findings.

2.1. Unusually-smooth surface of Atlas

More than 1,500 images of the satellites Pan and Atlas were obtained from the Narrow Angle Camera onboard Cassini spacecraft. They include 70 images with resolutions higher than 1km/pixel (as of January, 2011). Images of Atlas (Fig.15, 16a) obtained on June 12, 2007 have the highest resolution of ~320 m/pixel. I scrutinize all of these images to understand the surface conditions of both satellites (images of visible-near IR and infrared spectral ranges were also obtained, but these are at low resolutions (several dots for entire Atlas) and thus inappropriate to study surface conditions). Although the resolutions for images of Pan and Daphnis are limited, there is no significant difference in surface conditions as compared to Atlas.

All high-resolution images of Atlas suggest it has a smooth and featureless surface without any obvious craters (Charnoz et al. 2007). The lack of craters may indicate that (1) Atlas was formed in its present form and has never experienced any major impact; (2) the structure of Atlas is too fragile to allow a crater to maintain its original form; (3) the momentum of impact is efficiently absorbed by the rubble-pile structure (Hirata et al. 2009); or (4) craters existed until some kind of surface process erased them.

Based on the accretion scenario for the formation of Atlas, as discussed in the previous section, I find (1) is unlikely because (a) the radio occultation experiment of Voyager indicates that the A-ring is abundant in particles larger than km-size (e.g. Marouf et al. 1983), and therefore; (b) Atlas should have numerous craters

produced by impacts of km-size or larger particles at the time of accretion; (c) the current shape of Atlas should have developed at the time of accretion if no other surface process were active; and (d) other small satellites near the A-ring, such as Pandora and Prometheus, have numerous craters on their surfaces.

By scrutinizing the highest-resolution images, I newly identify a circular structure (Fig. 16b, 16c), which I interpret as a crater based on the following reasons (Fig. 16d): (a) the circular feature can be identified from its higher brightness, which implies the existence of a circular mound (interpreted here as a crater rim); (b) the brightness value of the circular mound appears to be constant along the illumination direction, which indicates the reflection angles (and thus the overall elevations) of the left- and right-side of the mound are the same; and (c) the center of the circular mound is in the shadow, which suggests the existence of a depression.

The identification of a crater is important because I can then rule out the possibilities of (2) and (3) in the above discussion. Therefore, the deficiency in craters likely implies that some sort of crater-erasing process has been active on the surface of Atlas.

There is the possibility that the deficiency of craters on Atlas is originated by its rubble-pile structure, whose size is almost identical to Roche lobe; large impacts may cause bulk reorganization, which completely remove the clue of impacts. However, this idea is difficult to reconcile with Prometheus and Pandora, which are expected to have rubble-pile structures and fill its Roche lobe (Porco et al. 2007) but still do have numerous craters, suggesting neither for the case of Atlas.

2.2. Resurfacing process on Atlas

The polar region of Atlas is characterized by both similarly-sized (a few km-scale) mounds and depressions, which might reflect the internal structure of Atlas. Porco et al. (2007) proposed that similarly-sized buried cores exist at the center of Atlas (Fig. 14). However, no topographic irregularities below a few km-scale can be found, which gives the smooth-looking surface even at the polar region. The important question I consider in this study

is why the smooth surface of the equatorial region is continuous to the polar region (Fig. 16b).

The illumination angle of the highest-resolution image (Fig. 16d) is unfortunately unknown; however, the illumination obviously comes from the left in this image. Due to the shape of the satellite, illumination angles are large enough at some areas to study surface states and structures. In general, no obvious roughness or shadows are found on the surface of Atlas except for the newly-identified crater (see above) and relatively large undulations at polar regions.

I propose that surface smoothness and the deficiency in shadows, even at the areas with large illumination angles, indicate that the surface of Atlas is covered by small particles. The continuity in the smoothness between the equatorial and polar regions can most easily be explained by that the surfaces of these regions are covered by the same materials in similar size-fractions. Particles that have accreted to the equatorial region also cover the cores of Atlas to form the bumpy polar region as suggested by Charnoz et al. (2007). However, accumulations of particles do not seem to occur globally; the current orbital shape of the A-ring indicates that particle accumulations likely concentrated at the region of the equatorial ridge, which is the main cause for the saucer-like shape of Atlas. Therefore, the continuity in the smoothness between the equatorial and polar regions indicates that fine particles on Atlas migrate and deposit through certain processes. Such processes may result in eliminating surface structures, including craters.

Migrations of materials on the surface of a small body are generally considered to be quite limited due to the lack of endogenic processes, water, and atmosphere. On small asteroids such as Eros and Itokawa, surface materials are redistributed by processes related to impact cratering, including re-deposition of ejecta material and migration of particles due to seismic shaking (e.g. Richardson et al. 2004, Miyamoto et al. 2007). Gardening effect due to continuous impacts of meteoroids may apparently contribute to resurface the airless bodies; for example, the locally smooth surfaces of the Moon and asteroids are sometimes explained by this

process (Sullivan et al. 2002). This may partially explain smooth local regions on some small saturnian satellites. For example, Calypso, Telesto, and Helene are located at the E-ring, which is consisted of μm-size particles (Kempf et al. 2008). Therefore, the surface smoothness of these satellites might be maintained by continuous impacts of micro-meteoroids. However, this does not seem to work for Atlas. It is true that Atlas is located in the Roche division, and thus, is expected to be continuously hit by the materials of Roche division, which is known to be not empty (Porco et al. 2005). However, Prometheus is also located in the Roche division, though the surface of Prometheus is not smooth. Therefore, I consider the unusual smoothness of Atlas cannot be explained by gardening effect due to continuous impacts of meteoroids.

Nevertheless, fine particles may migrate on Atlas due to the Coulomb force, which may cause levitation of fine particles on the surface of a small body when the particles covering the surface are electrically charged by the photoelectric effect (e.g. Whipple 1981). Once dust is levitated, horizontal migration might easily occur depending on the local gravitational and electrostatic states.

Dust levitation was first discovered on the lunar surface (e.g. Gold 1973, Whipple 1981) and suggested to occur on asteroids (e.g. Lee 1996, Colwell et al. 2005, Hughes et al. 2008). Lunar swirls, such as Reiner Gamma, which are albedo anomalies associated with strong crustal magnetic fields on the Moon, are considered to be resulted from migration due to dust levitation (Garrick-Bethell et al. 2011). Although generally considered as a minor surface process, the possibility of dust levitation has been implied for particles consisting the rings of Saturn (e.g. Nitter et al. 1998, Graps et al. 2008). In the following sections, I show that dust levitation likely plays a significant role in the inner saturnian system irrespective of its relatively large distance from the Sun (9AU – 10AU).

2.3. Dust levitation on Atlas

The surface of a solid body without atmosphere, such as an asteroid and the Moon, is charged positively because electrons are emitted by the photoelectric effect (Whipple 1981). On the Moon or an asteroid, this positive charge is neutralized by electrons provided

from solar wind plasma. However on Atlas, the solar wind plasma is minimized by the saturnian magnetosphere at around $2.28R_s$, where R_s is Saturn radii, while the positive charge on Atlas is neutralized by electrons provided by saturnian plasma. Thus, the electric charge at the surface of Atlas can also achieve the equilibrium state balanced between the supply of electrons from saturnian plasma and the photoelectron emission. In the following sections, I first determine the regions where dust levitation can occur in the saturnian system and estimate the largest size of particles that can migrate under the conditions of the surface of Atlas by following the theoretical model of Colwell et al. (2005). This theoretical model was developed for rocky objects, such as the Moon or asteroids, however, it could be acceptable for even icy satellites because the relative permittivity of an ice is not much different from that of a rock.

2.3.1. Conditions for dust levitation

When the surface of Atlas is charged positively, the electric charge per unit area of photoelectron emitted by photoelectric effects is given by,

$$\frac{dQ_s}{dt} = FY \exp\left(\frac{-e\Phi_s}{kT_{pe}}\right)\sin(i) \qquad , (1)$$

where Q_s is the electric charge on the surface, F is the number of the photons that can be ejected due to the photoelectric effect, Y is the photoelectron quantum efficiency, e is the quantum of electricity (e=1.602×10-19C), Φ_s is the electric potential of the surface, kT_{pe} is the photoelectron temperature, and i is the solar incident angle (here I use i=0 for simplicity). I adopt a well-known value for FY (2.8×10⁹/d² electron・cm⁻²・s⁻¹, where d is the distance from the sun; I use d=9.0AU, which is the Saturn's perihelion) and kT_{pe}/e=2.2eV (Willis et al. 1973).

Similarly, I estimate the electric charge provided from saturnian plasma as follows:

$$\frac{dQ_s}{dt} = n_{sp}\sqrt{\frac{kT_{sp}}{2\pi m_e}}\left(1 + \frac{e\Phi_s}{kT_{sp}}\right) \qquad , (2)$$

where n_{sp} is the electron density of the saturnian plasma, kT_{sp} is the average temperature of saturnian plasma, and me is the electron

mass (m_e=9.11×10^{-31}kg). By balancing equations (1) and (2), I obtain the electric potential of the surface, Φ_s, which depends on both n_{sp} and kT_{sp}.

Generally, smaller values of n_{sp} or kT_{sp}/e are favored for a dust to levitate (Fig. 17a, b). In addition, the critical values of n_{sp} and kT_{sp}/e are estimated to be in the order of 1.0 electron・cm^{-3} and 10eV, respectively. Based on Cassini's observations (Coates et al. 2005, Morooka et al. 2009, Gustafsson and Wahlund 2010), in this case, there are only two regions in the saturnian system where both of these values are below the critical values; 1) the region outside the orbit of Titan; and 2) the region that lies within A-, B-, and C-rings, including the orbits of Atlas and Pan (Fig. 17c). Cold and dense electron (extensived from 2.3Rs to ~10Rs) and hot and tenuous electron region (from ~5Rs to ~25Rs) are originated from the cryovolcanism on Enceladus and the atmosphere of Titan, respectively (Gombosi et al. 2009). In addition, cold and tenuous electron region around main ring is explained as a result of absorption of the plasma by particles of a dense main ring (Wahlund et al. 2005).

2.3.2. Largest particle-size for levitation

On Atlas, n_{sp} varies from 0.1 to 100 electron・cm^{-3} due to its orbit, while kT_{sp}/e is constantly a few eV regardless of the location in the orbit (Coates et al. 2005). To simplify the discussion, I adopt 0.1 electron・cm^{-3} and 2.0eV for n_{sp} and kT_{sp}/e, respectively. These values give the electric potential on the surface of Atlas, Φ_s, as large as 3.62V. On the other hand, the electric field on the surface of Atlas can be estimated by the following equation on the basis that photoelectron energy is in the Maxwellian distribution (Grard and Tunaley 1971):

$$E = \frac{4\Phi_s}{\sqrt{2}\lambda_D + z} \quad , (3)$$

where λ_D is the photoelectron's Debye length and is given as $\lambda_D = \sqrt{\dfrac{\varepsilon_0 k T_{pe}}{n_{pe,0} e^2}}$, where z is the height, ε_0 is the vacuum permittivity, and $n_{pe,0}$ is the number of photoelectrons on the surface. This number is

given by: $n_{pe,0} = \dfrac{2FY\sin(i)}{v_{pe}}$, where v_{pe} is the average photoemission

velocity; v_{pe} is 8.8×105m・s^{-1} when kT_{pe}/e=2.2eV.

The variation in the electric charge of drifting dust particles is given by the following equation:

$$\frac{dQ_d}{dt} = I_{pe} - I_e - I_{sp} \quad , (4)$$

where I_{pe} is the emission of photoelectron by the photoelectric effect, I_e is the collection of photoelectrons from the surface, and I_{sp} is the collection of electrons from saturnian plasma. I_{pe}, I_e, and I_{sp} are given, respectively, by the following three equations (Havnes et al. 1987), assuming that dust particles are spherical:

$$I_{pe} = \pi r_d^2 eFY \exp\left(\frac{-e\Phi_d}{kT_{pe}}\right) \;\; (\Phi_d > 0), \quad I_{pe} = \pi r_d^2 eFY \;\;\; (\Phi_d < 0) \quad , (5)$$

$$I_e = 4\pi r_d^2 en_{pe}\sqrt{\frac{kT_{pe}}{2\pi m_e}}\left(1 + \frac{e\Phi_d}{kT_{pe}}\right) \;\; (\Phi_d > 0), \quad I_e = 4\pi r_d^2 en_{pe}\sqrt{\frac{kT_{pe}}{2\pi m_e}}\exp\left(\frac{e\Phi_d}{kT_{pe}}\right) \;\; (\Phi_d < 0) \quad , (6) \text{ and}$$

$$I_{sp} = 4\pi r_d^2 en_{sp}\sqrt{\frac{kT_{sp}}{2\pi m_e}}\left(1 + \frac{e\Phi_d}{kT_{sp}}\right) \;\; (\Phi_d > 0), \quad I_{sp} = 4\pi r_d^2 en_{sp}\sqrt{\frac{kT_{sp}}{2\pi m_e}}\exp\left(\frac{e\Phi_d}{kT_{sp}}\right) \;\; (\Phi_d < 0) \quad , (7)$$

where r_d is the radius of particle, Φ_d is the surface electric potential of a dust particle, and n_{pe} is the density of photoelectron depending

on height. The value of n_{pe} is $n_{pe,0}\left(1 + z/\sqrt{2}\lambda_D\right)^2$ (Grard and Tunaley 1971).

When an equilibrium state is achieved, the left-hand side of equation (4) equals zero. In this case, I can analytically solve the equations (4), (5), (6), and (7) to obtain the surface electric potential of a given dust particle, Φ_d, depending on the height of the particle from the surface of Atlas.

Assuming that a dust particle is both spherical and homogeneously distributed, the mass and the electric charge of each particle are given by $4/3\pi r_d^3\rho_d$ and $4\pi r_d\varepsilon_0\Phi_d$, where r_d is the radius and ρ_d is the density of a particle. By balancing both the Coulomb ($4\pi r_d\varepsilon_0\Phi_d E$) and the gravitational ($4/3\pi r_d^3\rho_d g$) forces, I can estimate the largest size of any particle that can be levitated as follows:

$r_d = \sqrt{\dfrac{3\varepsilon_0\Phi_d E}{\rho_d g}}$, where g is gravity acceleration. I use ρ_d=900kg・m^{-3} as

the average density of ice and g=0.00082m・s^{-2} as the average

surface gravity acceleration. As a result, r_d simply reduces to a function of the particle height from the surface. The maximum radius that can be levitated is ~2.8μm, which stables at a height of ~46m (Fig. 18a).

2.3.3. Migration of a levitated particle

Particles near the surface should be charged individually and may acquire significantly different electrostatic potentials than the surface depending on such as illumination conditions and elevations. This as well as variations in local conditions (such as slope angles) might be major causes of particle migrations. Although a dust particle at a height below Debye length is negatively charged and interacts with the surface due to the Coulomb and gravitational forces, a dust particle above the height of the Debye length will be positively charged and thus can levitate for a long period because the Coulomb force cancels that of gravity.

Here I consider the acceleration forces of a levitated particle. For the simplicity sake, I assume the surface is perpendicular to the gravitational force, where the accelerations occur only in the vertical direction (Colwell et al. 2005):

$$\frac{d^2 z}{dt^2} = \frac{Q_d}{m_d} E - g \quad , \quad (8)$$

where m_d is the mass of the dust particle. Integrating equations (4) and (8), I can obtain the trajectories for particles (for example, those for a particle of r_d =1.0μm with five different speeds off the surface are shown in Fig. 18b). I find that if the particle is levitated at 0.1m/s, it stays within the dense part of the photoelectron layer and therefore remains negatively charged. Thus, such particle will immediately return to the surface due to both gravity and the electric forces. On the other hand, if a particle is levitated at slightly faster velocity (say, 0.2m/s), the particle becomes positively charged at the height of the Debye length and then accelerated upward. Afterward, the particle can suspend around 1km high for a long time. In summary, due to the small surface gravity on Atlas, a positively-charged particle can easily rise above the sheath even if it has a slower initial vertical velocity.

2.3.4. Dynamics of launching a particle

In the above model, an initial particle velocity is assumed without an initial particle charge (as assumed in the model of Colwell et al. 2005). Initial particle velocity is assumed to be given by the electrostatic force, however, in fact, uncertainty exists in the physical mechanism for particles to be released from the surface (e.g. Hartzell and Scheeres 2011). Assuming Gauss's law ($\sigma = \varepsilon_0 E_0$), the charge density per unit area (σ) on the surface of Atlas can be estimated to be 7.29×10^{-12} C・m^{-2} (=4.55×10^7 electron・m^{-2}), where E_0 is the electric field on the surface of Atlas and can be obtained by Eq.3 ($E_0 = 0.82$ V/m). Assuming that the surface is covered with μm-size dust particles, the number of μm-size particles in a unit area is larger than 10^{12}. In this case, the average electric charge per one particle is below the elementary charge, which means one particle takes one elementary charge while ten thousand particles are uncharged. Therefore, the electrostatic force becomes negligible for dust on Atlas at least theoretically. However, this is true even for the Moon and other airless bodies. Hughes et al. (2008) estimates that the largest strength of the nominal electric-field on the lunar surface is approximately 10 V/m. On the other hand, Hartzell and Scheeres (2011) shows that the electric field strength required to overcome the lunar gravity and cohesive forces (for separating a dust from the surface) is almost 1,000,000 V/m. In other words, the electric field strength theoretically required to loft a particle is significantly larger than observations, which remains unexplained. Therefore, Hartzell and Scheeres (2011) suggests that the charge on the dust particles is greater than that predicted by Gauss' law. In fact, Gauss' law simply gives the average charge on the dust particles, while the charge on a dust particle will vary in time depending on the emission of photoelectrons and the collisions with electrons from the plasma. Thus, there will be a non-uniform distribution of charges at the scale of a dust particle, while adhering to Gauss' law on the larger scale (Hartzell and Scheeres 2011).

The forces acting on a dust particle on the surface of airless bodies induce the gravity force ($F_{grav} = m_d g$), the surface cohesive force

(F_{co}), and the electrostatic force (F_{es}). The surface cohesive force can be described as $F_{co} = CS^2 r_d$, where C and S is constant, adopting the van der Waals force as the cohesive force. The electrostatic force is described as $F_{es} = Q_d E_0$, where Q_d is estimated to be $\pi r_d^2 \varepsilon_0 E_0$ though Gauss' law. Because the charging of dust particles is amplified beyond the levels predicted by Gauss' law as shown above, I use $Q_d = C_{amp} Q_d$, where C_{amp} is constant and is estimated to range from 4.04×10^4 to 1.04×10^9, by following the model of Hartzell and Scheeres (2011). Therefore, the electrostatic force is now described as $F_{es} = C_{amp} Q_d E_0$. Assuming that a particle can be separated from the surface when the electrostatic force (F_{es}) overcomes the gravity force (F_{grav}) and the surface cohesive force (F_{co}), electric field strength required to separate a particle from the surface (E_{req}) can be estimated as

$$E_{req} \geq \left[\frac{4}{3\varepsilon_0 C_{amp}} r_d \rho_d g + \frac{CS^2}{\pi \varepsilon_0 r_d C_{amp}} \right]^{1/2} , (9)$$

where the values of C_{amp}, C, and S are 5.01×10^6, 5.14×10^2 kg·s^{-2}, and 0.1~1, respectively, following the model of Hartzell and Scheeres (2011). Fig. 19 shows the electric field strength required to launch a particle from the surface (E_{req}) of the Moon, Eros, and Atlas as a function of particle's size. Note that, assuming the same surface electric fields, the particle on Atlas can be launched much easier than on the Moon and Eros. Even though electric field on the surface of Atlas is about one-tenth of those of the Moon and Eros, the minimum value of E_{req} in the case of Atlas is also one tenth of that of the Moon and Eros. Therefore, I consider that the electric field on the surface of Atlas is strong enough for launching of dust particles as happening on the Moon (and perhaps Eros).

2.4.　Global migration of dust particles on Atlas

I find that the electro-static levitations of particles would occur above the photoelectron layer. Because the scale of topographic irregularities on Atlas, such as a crater, is generally larger than the Debye length, the photoelectron layer should roughly follow the topography. I note that the generation of the photoelectron sheath partly depends on the solar incident angle,

which is locally controlled by topography. An ultimate example is the shadowed region, where sheath becomes absent and thus particles fall back to the surface even though the particles remain positively charged due to photoemission over a shadowed part of the surface. Importantly, particles on the shadowed regions are stable because the electrostatic repulsion cannot occur. Thus, a depression, such as a crater, likely traps dust particles migrated from the surrounding regions.

I also show that the size of the dust particle to migrate is a few µm. Although such phenomena occurs only for an extremely thin layer below the surface, a dust particle on the summer hemisphere of Atlas should be unstable for up to ~10 years, due to the orbital parameters of Saturn and the Sun (this occurs because the axial tilt of Saturn is 26.73 degrees while Atlas's orbital inclination to the equator plane of Saturn is 0.0). In other words, dust particles can migrate for a considerably longer time in the summer hemisphere because the summer hemisphere of Atlas is almost always dayside due to these orbital elements. On the other hand, in the winter hemisphere all of the particles should have settled to the surface. In this way, dust particles will migrate toward the winter hemisphere from the summer hemisphere. Therefore, a dust layer accumulates particles increasing its thickness, contrasting with the slowly-eroding dust layer in the summer hemisphere.

Migrations and depositions of particles may have been active cyclically for a long enough period to completely bury geological features on the surface of Atlas. If I assume only the uppermost particle can migrate in one saturnian season (10 years), the thickness of a mobile layer per one season is as thick as the typical particle size (say, ~10µm). Thus, on the dayside, particles may be eroded (as a result of particle migration) at the rate of 10µm per 10 years. This rate is fast enough to erase all of the craters on the surface of Atlas. Diameters of craters on Atlas cannot be larger than ~10km without being disrupted because the average diameter of Atlas is 30km. Assuming that the diameter-to-depth ratio of a crater is 10 to 1 (Melosh 1989), the depth of a large crater (say 1km

in diameter) is likely ~100m, which gives the volume of the crater as $3.93 \times 10^7 \text{m}^3$. This volume is equivalent to only 1cm depth of dust particles on the entire surface of Atlas, whose area is $3.70 \times 10^9 \text{m}^2$. Thus, if Atlas is resurfacing at the rate of 10μm per 10 years, this crater may be buried in only ~10000 years. Even large craters can be erased in a few tens of millions of years.
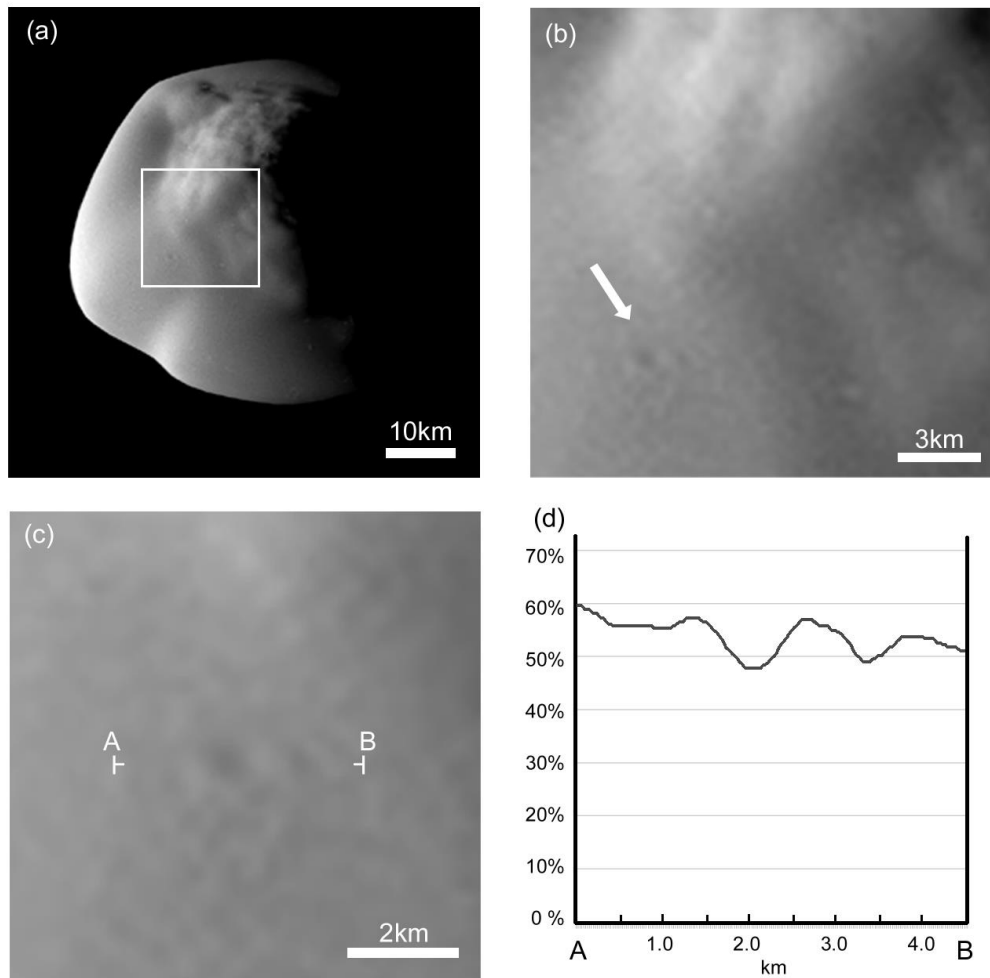
Figure 14 Crater on Atlas

(a) White box indicates the location of (b) (PIA08405). (b) Close-up of the transition area between the equatorial and polar regions showing continuity in the surface smoothness. The white arrow indicates the newly-discovered circular feature, interpreted here as a crater, whose close-up image is shown in (c). (c) Close-up image of the crater-like feature, whose brightness along the line between A and B crossing the center of the circular feature is indicated in (d). (d) Brightness (%) along the line between A and B shown in (c). Because the illumination comes from the left in (c), the brightness curve can be interpreted as results of topographic characteristics from A to B, such as a small mound (a crater rim), a large depression (the crater), a large mound (a crater rim), and a small depression (the shadow of the rim).
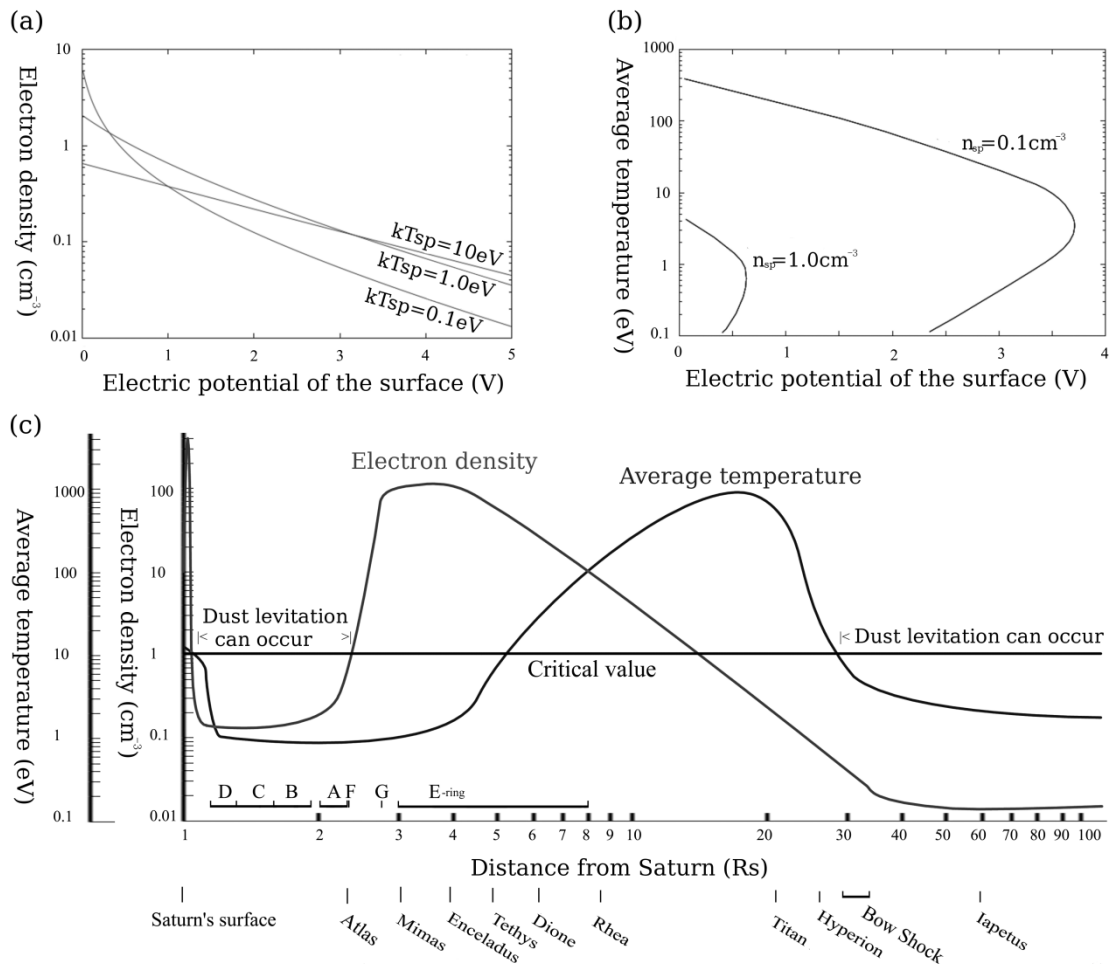
Figure 15 Electron density and temperature on Saturn system
(a) The electron density of saturnian plasma vs electric potential of surface with the assumed values of kT_{sp} as 0.1, 1.0, and 10eV. (b) The average electron temperature of saturnian plasma vs electric potential of surface with 0.1 or 1.0 electron·cm^{-3} for n_{sp}. When n_{sp} is larger than 10 electron·cm^{-3}, electric potential of surface becomes zero. (c) Approximate observation value of the electron density and the average electron temperature of Saturn system. The regions where both of these are smaller than the critical value for dust levitation are limited to the regions around the A-, B-, and C-ring and outside the orbit of Titan.
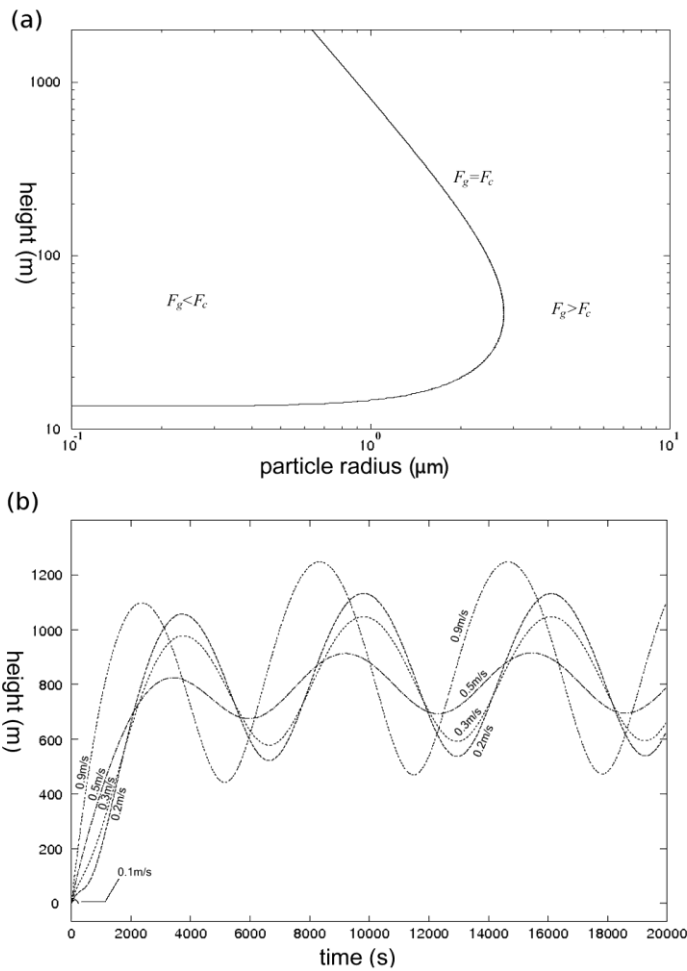
Figure 16 The fate of a levitated particle
(a) Comparison of the gravity force (F_g) and the Coulomb force (F_c) as functions of heights and particle size. (b) The fate of particles levitated from the surface (the heights of particles are shown as a function of time for the case of $r_d = 1.0\mu m$ at the solar noon on Atlas with different initial velocities). All particles are accelerated up above the photoelectron layer except a particle with 0.1m/s, which remains within the photoelectron layer.

Figure 19 The electric field strength required to launch a particle from the surface.

The electric field strength (E_{req}) of the Moon, Eros, and Atlas as a function of particle's size. I assume the density of particle in the Moon and Eros as 3500kg・m^{-3}. I use g= 1.622m・s^{-2} and 0.0055m・s^{-2} as the average surface gravity acceleration of the Moon and Eros, respectively.

3. Discussions of satellites of A-ring and F-ring region

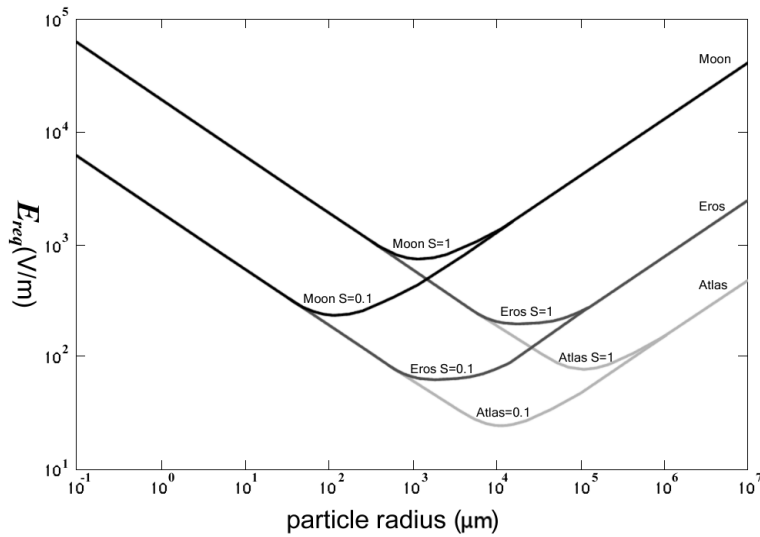I show that there are only two regions in the saturnian system where small particles on the surface can be charged and levitated, such as 1) the region outside the orbit of Titan and 2) the region that lies within A-, B-, and C-rings, including the orbits of Atlas and Pan. I note that the physical model adopted here is also applicable for many other airless bodies in the solar system or Saturn system. Another important issue, which makes Atlas different from other bodies, is the amount of dust. If dust is not supplied from other processes, the amount of dust on the surface of a body is limited due to the escapement of dust from its tiny gravity, the solar radiation pressure, potentially gravitational perturbation, or other reasons. In fact, a dust of Eros and Itokawa are quite limited or only locally concentrated on their surfaces (e.g. Richardson et al. 2004, Miyamoto et al. 2007). On the other hand, the cases of satellites of A-ring and F-ring regions, Pan, Daphnis, Atlas, Prometheus, and Pandora, are different; my geological investigation indicates that fine particles likely cover the entire surface of satellites. Particles covering satellites of A-ring probably come from A-ring (e.g. Porco et al. 2007, Charnoz et al. 2007), which contains many particles smaller than several tens of micro meters as following reasons.

An individual ring particle cannot be directly observed, however, these macroscopic properties can be seen as the entirely ring property. At the same time, the ring properties reflect the property of an individual ring particle. Cassini space mission, Voyager space mission, and Hubble space telescope reveal numerous features of ring system. The physical size of ring particles can be estimated using the radio and/ or staller occultation experience. The Voyager radio occultation in 1980 and the Earth-based 28 Sgr stellar occultation in 1989 conclude that 1) particle size distributions range 1 cm to 10 m, 2) these power laws are close to 3, and 3) μm-size particles are few (Tyler et al. 1983,

Marouf et al. 1983, Zebker et al. 1985, French and Nicholson 2000). Therefore, there are no dust particles in ring, at least alone. On the other hand, analyses of the ultraviolet, visual, and infrared spectra of ring conclude that ring particles range a few µm to a few ten µm (Clark et al. 1986, Doyle et al. 1989, Nicholson et al. 2008). The spectra features can be considered to show that the surface of ring particles consists of more dusty particles even though the possibility that these observations indicate the frosty surface or roughness surface of ring particles cannot rule out. In addition, the thermal inertia values of ring particles derived from recent Cassini observation support show ring particles has deep dusty layers. Ring particles cool down when they cross the shadow region of Saturn or saturnian rings. After ring particles pass through the shadow region, ring particles heat up again due to the solar radiation. Observed these thermal changes, the thermal inertia values can be estimated. The analyses of the thermal inertia values show that 1) ring particles are likely to have a deep dusty regolith layer, and 2) even small particles with the fast rotation period also have dusty regolith layers (Morishima et al. 2011). These results of the thermal inertia indicate ring particles have not the frosty surface or roughness surface but regolith layers consisting of dusty particles. Also, the internal density of a ring particle is estimated using the observation of non-axisymmetric ring brightness and N-bodies simulation. Non-axisymmetric brightness in reflected light of the A- and B-ring is observed, which indicates the existence of micro-structure due to the self-gravity of ring particles (e.g. Cuzzi et al. 2010). Dynamical simulations for formation of these wake structures in the A and B rings show that the internal density of ring particles is close to the half of ice (Salo et al. 2001, Stuart et al. 2010), which indicates that the porosity of a ring particle is so high. Based on these observations, Cuzzi et al. (2009) summarizes actual ring particles are likely to be chunky aggregates or dense grape clusters consisting of dusty particles. These aggregates are incessantly disrupted and/or unionized due to due to collisions against each other and some interactive forces, such as the Van der Waals force. Therefore, A-ring is probably enriched in dusty

particles, whose size-fraction is sufficiently small enough to be electro-statically levitated when deposited on the surface of satellites of A-ring and F-ring regions.

As a result, I conclude that the smoothness of Atlas's surface is formed by the special environments, where 1) satellites of A-ring and F-ring regions has the source of a large amount of dusty particles, and 2) satellites of A-ring region are located at inner saturnian magnetosphere characterized by lower electron density and cooler electron temperature. In addition, these different environments cause the different features between satellites of A-ring regions and satellites of F-ring regions.

Part 3

Janus and Epimetheus, located within the orbit of Mimas, have a co-orbital ring system. This part discusses the geological features of Janus and Epimetheus and their interaction with the ring system.

Spectral data and high-resolution images of the satellites are obtained by recent Cassini mission. Through detailed investigations of high-resolution images, I find that both satellites consist of distinct two terrains, dark and bright terrains. The dark terrain is identified on gravitational lowlands all over the satellites. The dark terrain on both Janus and Epimetheus are similar in terms of their (1) flat smooth surfaces, (2) albedos darker than surrounding bright terrain, (3) sharp edges, (4) depths as deposits, and (5) bluer colors. I find that this dichotomy may be explained by the accumulation of Janus-Epimetheus ring.

1.   Janus and Epimetheus

Janus and Epimetheus are small saturnian satellites located within the orbit of Mimas. The satellites are known as the co-orbital moons, coexisting at the same orbit. Janus and Epimetheus were first discovered by Dollfus (1967) and Walker (1967), respectively. However, the satellite observed by Walker (1967) was regarded as Janus until Fountain and Larson (1978) pointed out that two distinct objects existed at the horseshoe orbit. Such unusual orbit was predicted but not detected within the Solar System until Janus-Epimetheus system was discovered.

Also, the Cassini spacecraft discovers a tenuous ring at the vicinity of the satellites, Janus/Epimetheus ring (hereafter JE-ring). JE-ring is a faint dusty ring, whose semi-major axis ranges between 149,000 and 154,000 km from the center of Saturn (Porco et al. 2006b). The ring particles are considered to be originated from Janus or Epimetheus.

The densities of the satellites are lower than ice, which means these satellites have high porosity (Table 5). Assuming pure ice, porosities of these satellites are around 30%, which is close to the values of Asteroid Eros or Ida (Belton et al. 1995). This value indicates Janus and Epimetheus have either immense monolithic structure with cracks or rabble pile structure. The interior pressure of a satellite is not enough to melt own materials (Stooke and Lumsdon 1993). Previous work (Stooke and Lumsdon 1993) suggests that, after a larger satellite have been disrupted in early Saturn system, aggregates of breccia have been formed, resulting in formations of Janus and Epimetheus.

The surface features of these satellites resemble each other. Janus and Epimetheus are observed by Voyager and Cassini spacecraft, which reveal a lot of surface features, such as grooves (Morrison et al. 2009) and heavily-cratered surfaces (Stooke 1993, Stooke and Lumsdon 1993). This high crater density on the satellites indicates the satellites may be as old as several Gy, even though cratering rate on small inner satellites remains uncertain.

Janus and Epimetheus are poorly-understood satellites. In

this part, I report and discuss their geological features. In detail, I find that non-uniform brightness distribution exists on their surfaces, the dark terrain and the bright terrain (Fig. 20). I show the nature of these terrains in the former part of Part 3. Moreover, I find the accumulation of the JE-ring may play a role to form the dark terrain, which is shown in the latter part of Part 3.
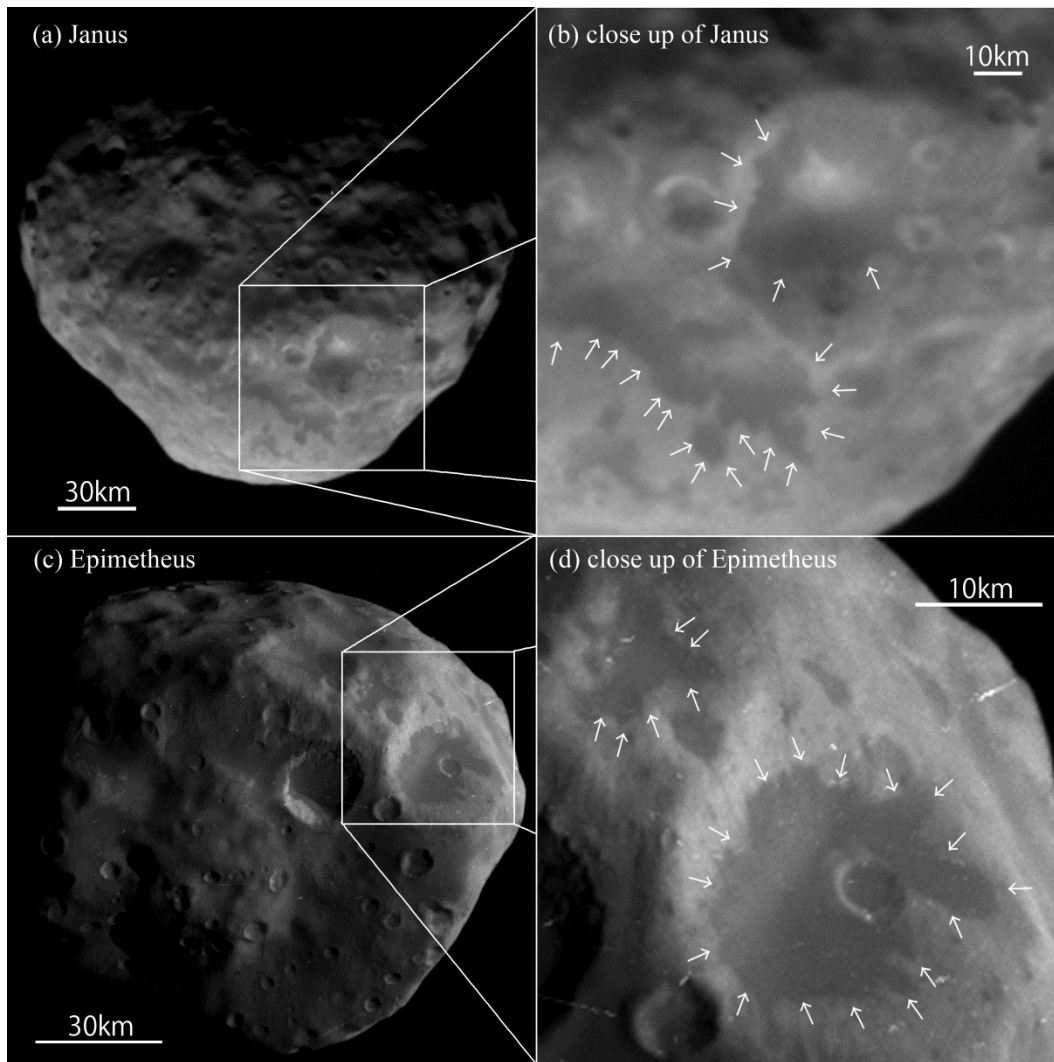
Figure 17 The bright terrain and the dark terrain.
High-resolution images of (a, b) Janus (N1627319821) and (c, d) Epimetheus (N1575363079). (b) and (d) are close up images of (a) and (c). White arrows indicate the boundary between the bright terrain and the dark terrain.

2. Geological study

I start with an overview of the available Cassini ISS and VIMS images by 2010. In detail, I carefully examine 208 images for Janus and 64 images for Epimetheus. Moreover, I analysis 200 images for Janus (Table 8) and 40 images for Epimetheus (Table 8) obtained by VIMS camera. VIMS camera consists of two channels, visual and infrared. The VIMS Visual instrument possesses 96 spectral channels that measure radiation between 0.35 and 1.05 µm, while the VIMS infrared instrument operates between 0.86 and 5.2 µm and collects reflected light in 256 spectral channels. I use the ISIS3 software to radiometrically calibrate VIMS data and ISS images.

2.1. Dark terrain and Bright terrain

The normal reflectance of the dark terrains is roughly 0.81~0.88 and 0.75~0.84 times brighter than the bright terrains on Janus and Epimetheus, respectively. Dark deposits are often identified on the surface of saturnian satellites, for example Hyperion and Iapetus, which are considered to be formed by the exogenic contaminations (e.g. Stephan et al. 2010). However, previous spectral study (Buratti et al. 2010) shows that Janus and Epimetheus don't contain the spectra identified on Hyperion or Iapetus, such as the absorption bands of CO_2.

The dark terrain distributes on the gravitational lowlands and each dark terrain is isolated over all satellite. On the other hand, the bright terrain distributes on the gravitational highland and these regions are identified to have the continuity among each other. The dark terrains on the satellites appear flat smooth surface and sharp edge. In detail, the surface of the dark terrain shows less-undulation of brightness value (even regions with the large illumination angles) while the bright terrain generally appears numerous small undulations. In addition, the transit regions between bright and dark terrains may be quite narrow, at most ~100 m.

2.2. Color ratio and spectral data

Color ratio shows that the dark terrain is slightly bluer than

that of bright terrain (Fig 21). Here I use the ratio of the normal reflectance at 500 randomly selected pixels through the IR3 (953nm) filter, GRN (563nm) filters, and UV3 (340nm) filter onboard Cassini ISS camera. The color ratio of IR3/GRN of the dark terrain is not much different from the bright terrain while the color ratio of UV3/GRN of the dark terrain is larger than that of the bright terrain. In addition, the average ratio of IR3/UV3 of the bright terrain is 1.73 for Janus and 1.75 for Epimetheus while that of the dark terrain is 1.67 for Janus and 1.66 for Epimetheus.

I also study the VIMS data. I note that the VIMS images of both satellites are generally too low resolution to distinguish between the dark and bright terrains (generally a few pixels in the image). Therefore, I use the images obtained by ISS camera at the same time in order to estimate the imaged regions (Fig. 22a, d). Furthermore, I calculate the average of total pixels of the VIMS images obtained at the same flyby (Fig. 22b, c, e, f), which can show the typical spectral features of the imaged regions. Especially, Epimetheus is the best example because I can compare the spectra of Epimetheus taken from trailing side in Mar. 30 2005, July 14 2005, and Apr. 7 2010 (where is covered by the bright terrain) and south pole in Dec. 3 2007 (where is covered by the dark terrain) in high resolutions (Table 9). As a result, I cannot identify the differences between bright and dark terrains, for example the absence of NH_3 or CO_2 absorption bands and the depth of H_2O absorption, even though these contain un-negligible measurement deviation. VIMS spectra indicate that the compositional differences between the bright and dark terrains may not be large.

2.3. Distributions of dark terrains

To investigate the distribution of the dark terrain, I first develop the cylindrical projection map of both satellites (Fig. 23a, b) (see Appendix). Then, I use 25 images for Janus (Table 6) and 4 images for Epimetheus (Table 7). Note that the entire surface of Janus, except for sub-Saturn side and north polar region, is imaged by Cassini. Also, the imaged regions of Epimetheus are limited to either the trailing side or the south polar region. The maps show that the majority of the dark terrain on Janus appears the

equatorial region of anti-Saturn side while the dark terrain on Epimetheus mostly appears on the south polar region.

2.4.　Origin of the dark terrain

　　　　The difference between the dark terrains on Janus and Epimetheus, for example colors, spectra, and surface features, cannot be identified. The similarity indicates the common origin. Also, I propose that the dark terrain is made of fine particles. This is because (i) fine particles have generally small friction angles, which are easy to form the flat surface, (ii) the differences of fiction angles between particles in the dark and bright terrains are easy to form the shape boundary due to sorting processes, and (iii) bluer color implies the Rayleigh scattering effect due to the existence of μm-sized particles. On the other hand, the distribution of the dark terrain may be explained by the accumulation of Janus-Epimetheus ring particles as following reason.

(a) Color ratio on Janus

(b) Color ratio on Epimetheus
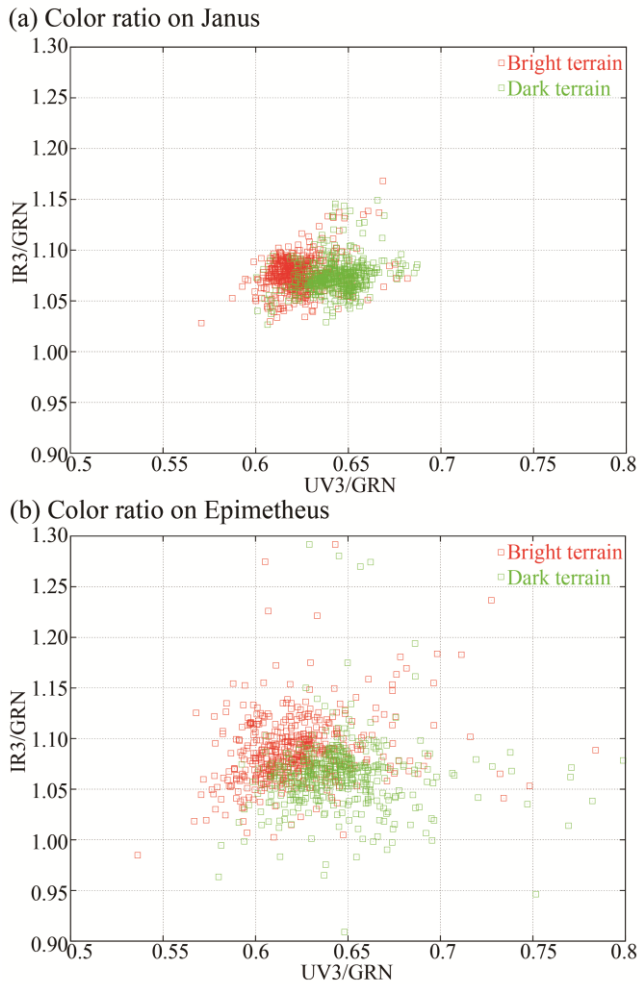
Figure 18 Color ratio of the dark and bright terrains.
Dots represent relative reflectance at randomly selected pixels (see text). Red and Green dots represent the dark terrain and the bright terrain, respectively. Vertical axis means the ratios of the normal reflectance through IR3 (953nm) and GRN (563 nm) filters of Cassini ISS camera. Horizontal axis means ones through UV3 (340nm) and GRN (563 nm) filters. Here I use N1627323131, N1627323305, and N1627323227 for Janus and N1575363109, N1575363139, and N1575363199 for Epimetheus.
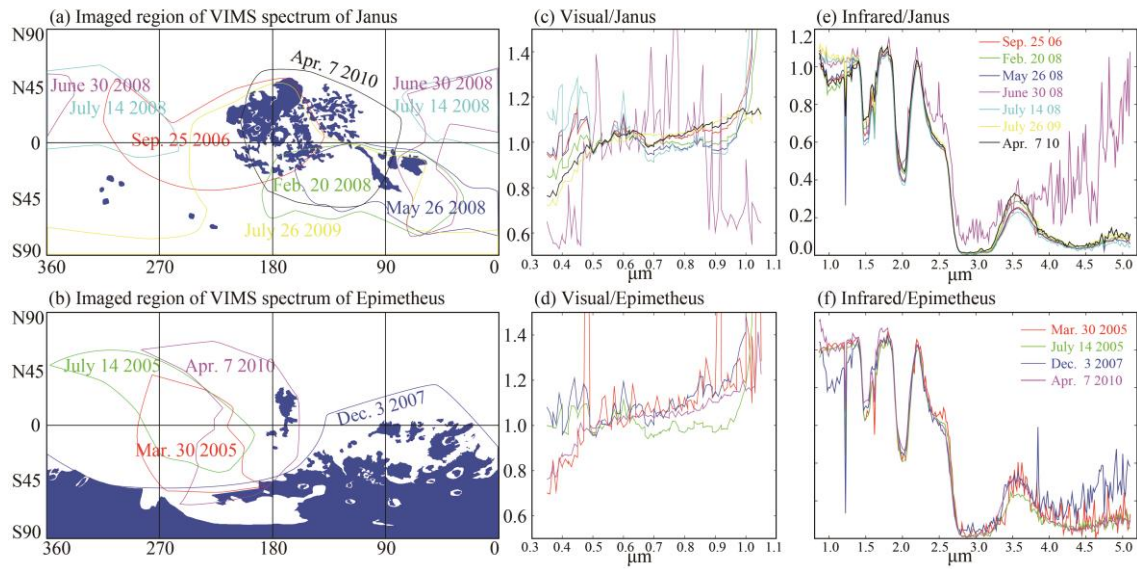
Figure 19 Spectral data of Janus and Epimetheus

Imaged regions of spectral data of (a) Janus and (b) Epimetheus. The imaged region in each flyby (its date is shown in the same color) is shown in closed-lines. Here I show 7 flyby listed in Table 8 for Janus and 4 flyby listed in Table 9 for Epimetheus. Blue regions represent the distribution of the dark terrain, which also shows Figure 23. Visual and Infrared spectral features are normalized these at 0.55 µm and 2.23 µm, respectively. Legends of Infrared share with these of Visual.

Figure 20 The cylindrical projection map of Janus and Epimetheus.
Blue regions represent the distribution of the dark terrain on Janus
and Epimetheus.

Table 6 Images of Janus used for developing the cylindrical projection map

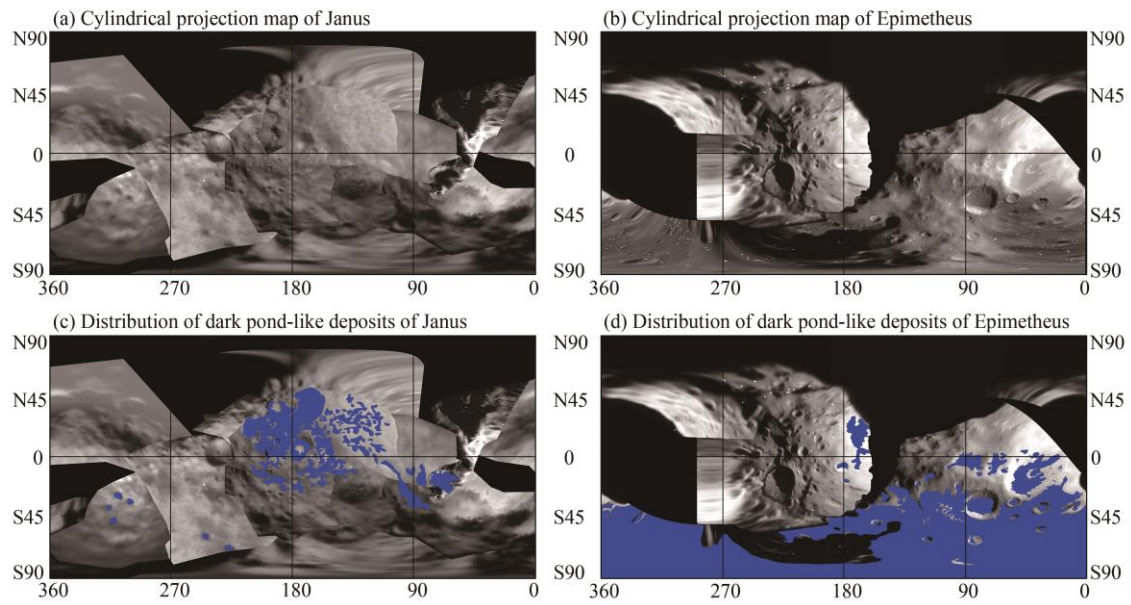| Image number	Time (UTC)	Sub-Cassini		Sub-Solar		Resolution	Range
		Lat.	Lon.	Lat.	Lon.	(km/pixel)	(km)
N1524964907	Apr. 29 2006	-0.1	232.8	-11.8	233.9	1.288	216294
N1524966188	Apr. 29 2006	-0.1	239.2	-11.7	241.9	1.354	227329
N1537919879	Sep. 25 2006	10.1	162.8	-10.0	188.5	0.822	137976
N1537921114	Sep. 25 2006	12.9	172.3	-10.1	195.7	0.857	143908
N1537922721	Sep. 25 2006	15.9	184.7	-10.2	205.6	0.926	155456
N1537923147	Sep. 25 2006	16.8	188.0	-10.2	208.1	0.948	159214
N1582238183	Feb. 20 2008	-62.5	88.5	-5.1	10.0	1.011	169684
N1582240507	Feb. 20 2008	-65.5	96.1	-5.1	23.0	1.096	183920
N1589742988	Mar. 17 2008	31.1	321.1	-4.5	32.0	2.086	350212
N1590458717	May 26 2008	-66.4	302.4	-4.5	6.0	1.091	183182
N1590461157	May 26 2008	-65.2	317.3	-4.4	20.0	1.269	213014
N1593508083	June 30 2008	14.1	97.1	-4.1	295.3	0.284	47705
N1593508487	June 30 2008	8.7	99.7	-4.1	297.9	0.245	41053
N1593509479	June 30 2008	-12.6	106.7	-4.1	303.9	0.181	30323
N1593509659	June 30 2008	-18.1	108.1	-4.1	305.0	0.177	29782
N1593509823	June 30 2008	-23.5	109.5	-4.1	306.1	0.177	29761
N1594708901	July 14 2008	63.4	322.8	-3.9	299.5	1.550	260174
N1627318239	July 26 2009	-33.5	162.8	0.0	84.5	0.618	103674
N1627318975	July 26 2009	-31.0	168.3	0.0	88.5	0.598	100310
N1627319821	July 26 2009	-27.7	174.6	0.0	94.2	0.579	97225
N1627323065	July 26 2009	-13.4	198.4	0.0	113.0	0.572	95993
N1627323901	July 26 2009	-9.8	204.0	0.0	118.0	0.589	98915
N1627324437	July 26 2009	-7.7	207.5	0.0	120.8	0.605	101512
N1630068448	Aug. 27 2009	-2.9	74.2	0.2	23.2	1.585	266061
N1649342351	Apr. 7 2010	-1.0	143.8	2.2	79.4	0.446	74844

Table 7 Images of Epimetheus used for developing the cylindrical projection map

| Image | Time (UTC) | Sub-Cassini | | Sub-Solar | | Resolution | Range |
		Lat.	Lon.	Lat.	Lon.	(km/pixel)	(km)
N1490836932	Mar. 30 2005	0.1	206.3	-20.2	278.3	0.448	75198
N1500072080	July 14 2005	23.3	214.1	-16.3	251.9	0.524	87877
N1575363079	Dec. 3 2007	-33.8	116.7	-7.0	358.9	0.221	37177
N1649345705	Apr. 7 2010	-1.0	201.6	3.3	113.1	0.516	86632
N1649347561	Apr. 7 2010	-0.8	205.6	3.1	129.4	0.599	100480
N1649348312	Apr. 7 2010	-0.8	207.3	3.0	135.4	0.637	106995

Table 8 Spectral images of Janus obtained by VIMS

| Image | Time (UTC) | Total pixel number | |
		Visual	Infrared
v1537919388-1537923173	Sep. 25-26 2006	129	101
v1582235504-1582240921	Feb. 20 2008	189	91
v1590456690-1590461135	May 26 2008	145	79
v1593506582-1593509815	June 30 2008	34	34
v1594708738-1594710035	July 14 2008	91	41
v1627318261-1627324363	July 26 2009	229	538
v1649342677-1649345695	Apr. 7 2010	225	204

Table 9 Spectral images of Epimetheus obtained by VIMS

| Image | Time (UTC) | Total pixel number | |
		Visual	Infrared
v1490836110-1490836433	Mar. 30 2005	4	12
v1500071963-1500073059	July 14 2005	24	56
v1575362963-1575363931	Dec. 3 2007	96	96
v1649345758-1649350288	Apr. 7 2010	36	72

3. Interaction with Janus Epimetheus ring

3.1. Theoretical view of satellites and ring particles

The accumulation of JE-ring particles may be theoretically expected to preferentially deposit on the near and far side of Janus and Epimetheus. In this section, I discuss the relative amounts per unit area of impactors supplied from JE-ring material on Janus and Epimetheus.

Here I define that the orbit of Janus has P_j and A_j for the periapsis and apoapsis distances, respectively, as shown in Fig. 24. Based on e.g. Smulsky and Smulsky (2012), the orbit of Janus in a polar coordinate system with origin at the center of planet can be described as

$$r_j = \frac{P_j}{(\alpha_j+1)\cos\varphi - \alpha_j},$$

where r_j means the radial distance, φ means the polar angle ($\varphi = 0$ in the perihelion of Janus), and α_j is the constant defined as

$$\alpha_j = -\frac{A_j+P_j}{2A_j} \ .$$

Furthermore, the radial velocity ($v_{r,j}$) and transversal velocity ($v_{t,j}$) of Janus (when the distance between Saturn and Janus is r_j) can be described as

$$v_{r,j} = \pm v_{p,j}\sqrt{(\alpha_j + 1)^2 - \left(\alpha_j + \frac{P_j}{r_j}\right)^2} \quad (v_{r,j} > 0 \text{ in } 0 < \varphi < \pi;\ v_{r,j} < 0 \text{ in } \pi < \varphi$$

$< 2\pi$) and (10)

$$v_{t,j} = \frac{P_j v_{p,j}}{r_j}, \text{ respectively, (11)}$$

where $v_{p,j}$ means the velocity in the perihelion point of Janus. $v_{p,j}$ can be obtained by

$$v_{p,j} = \sqrt{-\frac{GM_s}{\alpha_j P_j}},$$

where G and M_s mean the gravity constant and the mass of Saturn, respectively.

Next, I assume a typical ring particle which has P_p and A_p for the periapsis and apoapsis distances, respectively. Then, the orbital equation of the particle in the same coordinate system can be described as

$$r_p = \frac{P_p}{(\alpha_p+1)\cos(\varphi-\theta)-\alpha_p},$$

where r_p means the radial distance, θ means the phase angle (in other ward, $\varphi = \theta$ in the perihelion of the particle), and α_p is the constant defined as

$$\alpha_p = -\frac{A_p+P_p}{2A_p}.$$

Furthermore, the radial ($v_{r,p}$) and transversal ($v_{t,p}$) velocity of Janus when the distance between Saturn and Janus is r_p can be described as

$$v_{r,p} = \pm v_{p,p}\sqrt{\left(\alpha_p+1\right)^2 - \left(\alpha_p+\frac{P_p}{r_p}\right)^2}$$

($v_{r,p} > 0$ in $0 < \varphi\text{-}\theta < \Pi$; $v_{r,p} < 0$ in $\Pi < \varphi\text{-}\theta < 2\Pi$) and (12)

$$v_{t,p} = \frac{P_p v_{p,p}}{r_p},\text{ respectively, (13)}$$

where $v_{p,p}$ means the velocity in the perihelion point of Janus. $v_{p,p}$ can be obtained by

$$v_{p,p} = \sqrt{-\frac{GM_s}{\alpha_p P_p}}.$$

Hence, I can describe the relative velocity when a particle collides toward Janus for

$$v_{imp} = (v_{r,j} - v_{r,p}, v_{t,j} - v_{t,p}),\text{ (14)}$$

where $v_{r,j} - v_{r,p}$ means the relative radial velocity and $v_{t,j} - v_{t,p}$ means the relative transversal velocity.

JE-ring particles have the similar orbit to Janus and Epimetheus. The particles typically have the same apsis distance with those of the satellites. I assume that P_p, and A_p are equal to P_j and A_j, respectively. In this case, r_p should be equal to r_j when the particle collides toward Janus. Then, from the Eq, 10, 11, 12, and 13, I can obtain $v_{t,j}=v_{t,p}$ and $|v_{r,j}| = |v_{r,p}|$ (if $v_{r,j} < 0$, then $v_{r,p} > 0$; if $v_{r,j} > 0$, then $v_{r,p} < 0$). Hence, from the Eq. 14, I can obtain the radial

and transversal directions of the relative velocity for

$$v_{imp} = \left(\pm 2v_{p,j} \sqrt{\left(\alpha_j + 1 \right)^2 - \left(\alpha_j + \frac{P_j}{r_j} \right)^2}, 0 \right) . (15)$$

The relative velocity of the transversal direction is offset, which means that particle collides toward the near side or far side of Janus. From the Eq. 15, $|v_{imp}|$ ranges from 0 to 240 m/s, where I use 150,500 km and 152,500 km for P_j and A_j, respectively. Note that, if the phase angle (θ) is less than 5 degree (or 355° < θ), which means the orbit of the particle is almost the same as that of Janus. In this case, the collisions should occur in quite low velocity (at most 10 m/s) from any directions. Even if I assume the maximum of eccentricity of a ring particle (P_j = 149,000 km and A_j = 154,000 km), $v_{t,j} \cdot v_{t,p}$ is not large (at most 130 m/s). In this case, if the phase angle is 320° > θ > 40°, the direction of a particle is limited within 45° from the sub-Saturn or anti-Saturn points. The case of Epimetheus is a little bit different from that of Janus because the large inclination of Epimetheus (~0.3) is expected to generate the collisions toward the south pole or north pole of Epimetheus.

The distribution may be consistent with the distribution of the dark terrain. To reconfirm this view, I perform the numerical simulations of interactions between JE-ring and satellites.

3.2.   Numerical simulation of Janus-Epimetheus ring

Previous study of numerical simulation of JE-ring (Williams and Murray 2011) shows that almost all JE-ring particles should collide with Janus or Epimetheus for a decade, which indicates that Janus and Epimetheus temporary feed JE-ring. On the other hand, I calculate the amount of impactors supplied from JE-ring material on a given region of the satellites.

First, I reconstruct the orbital motion of JE-ring particles in the Janus and Epimetheus system. To construct the complex motions of Janus and Epimetheus, I define them as their actual values from Jan. 1 2000 to Dec. 31 2011, which are referred from NASA's Navigation and Ancillary Information Facility (NAIF). Detail dynamics of the ring particles are quite difficult because of a lot of forces, such as the gravity of satellites, the Lorentz force of

saturnian magnetosphere, and the solar radiation pressure. Especially, the Lorentz force is known to be fairly effective to small particles (1µm or smaller). However, I am obliged to ignore the Lorentz force and the solar radiation pressure because we understand neither the composition nor the typical size of JE-ring particles. I note that the results of my simulation may become markedly different if we assume quite small particles. In any case, both the gravity of ring particles and the collisions between ring particles are also negligible because JE-ring is quite tenuous. Then, I can describe the equation of a ring particle's motion as

$$\frac{d^2\mathbf{r}}{dt^2} = -GM_s \frac{\mathbf{r}}{|\mathbf{r}|^3} - GM_j \frac{\mathbf{r}-\mathbf{r_j}}{|\mathbf{r}-\mathbf{r_j}|^3} - GM_e \frac{\mathbf{r}-\mathbf{r_e}}{|\mathbf{r}-\mathbf{r_e}|^3}, \quad (16)$$

where $\mathbf{r}$, $\mathbf{r_j}$, and $\mathbf{r_e}$ mean the position vector with their origin at the center of Saturn of the ring particle, Janus, and Epimetheus, respectively, and M_j and M_e mean the mass of Janus and Epimetheus, respectively. To solve this ordinary differential equation, I use the Runge–Kutta method.

The relative velocity between a JE-ring particle and the satellites is generally ~200 m/s (see section 3.4). Therefore, I define the time interval as 60 second. The relative position of particles move 6 km in a step, whose values are much smaller than the sizes of the satellites. Therefore, 60 second is sufficient to my purpose. I use 50000 particles as initial values, which have the semi major axis ranging from 149,000 to 154,000 km and the keplerian velocity of its orbit. I show the locations of ring particles and satellites in every 100,000 step (equal to 6,000,000 seconds) to Fig. 25 and 26. I define the sphere with the mean radius of satellites as the shape of the satellites. Then, I assume that the particle moving into the sphere means that particles collide with the satellite. I define the particle which collides satellites will be removed in this simulation. As a result, about 20 % of all particles have been removed for a decade. The directions of particles collided with the satellites are shown in Fig. 27. The collisions concentrate to the near and far side of Janus and the polar regions of Epimetheus, which is consistent with section 3.1.

3.3. Impactors flux on the satellites

Next, I calculate the relative mass of impactors supplied from JE-ring material on a given area. This means the depositional rate. Because I assumed the sphere as the shapes of the satellites, I can regard an collisional event as a particle passing through the circle with area πr_s^2 perpendicular to the directions of the particle's motion, where r_s means the mean radius of the satellite. Then, I can describe the probability which a particle collides to a given unit area of the circle as $1/\pi r_s^2$. Therefore, assuming that a particle (m_p for its mass; $\mathbf{t}$ for its direction unit vector) collides to a given sufficiently-small area on the satellites (s for its name; A_s for its area; $\mathbf{s}$ for its unit normal vector), I can obtain the statistically expected mass ($E(s,t)$) of the surface regolith supplied by the particle on the small area as

$$E(s, t) = \frac{m_p}{\pi r_s^2} A_s (\mathbf{s} \cdot \mathbf{t}) \quad (\mathbf{s} \cdot \mathbf{t} > 0) \text{ or}$$

$$E(s, t) = 0 \quad (\mathbf{s} \cdot \mathbf{t} < 0),$$

where I define $\mathbf{s}$ has the direction from outside to inside of the satellite. Here $\mathbf{s} \cdot \mathbf{t}$ means the incident angle between the direction of the particle and the small area. Hence, the statistically expected mass of impactors supplied by all JE-ring particles on a given small area, s, can be described as

$$E(s) = \sum_t E(s, t). \text{ (17)}$$

Assuming that A_s is the unit area (1 km^2), all particles of JE-ring has the same mass, the total amount of impactors supplied from JE-ring material over the entire surfaces of both satellites is 1 kg, and the unit vector $\mathbf{s}$ on a given area is based on the shape model developed by Stooke and Lumsdon (1993) and Stooke (1993), I can show the mass of impactor flux per unit of area (kg·km^{-2}) to Fig. 28.

3.4.   Erosional or depositional flux

An impactor is expected to cause either deposition or erosion, depending on the impact angle and velocity. The distribution of impact velocities is shown in Fig. 29. The escape velocity of Janus and Epimetheus are 53.2 m/s and 34.8 m/s, respectively. The velocities of impactors are typically a few times as rapid as the escape velocities. These impactors sensitively contribute to

deposition or erosion of the satellites' regolith, depending on the impact angle. According to experimental studies about the collision of an impactor with a few hundred m/s toward a flat powdered surface, the total kinetic energy of ejecta is less than 1 % for that of the impactor (e.g. Hartmann 1985). Then, the maximum velocity of ejecta is at most 10% as rapid as that of the impactor in the case of normal impact (> ~30°) (Hartmann 1985) while the maximum velocity of ejecta is at most 64% as rapid as that of the impactor in the case of the oblique impact (< ~30°) (Yamamoto 2002). The velocities of ejecta are close to the escape velocity of the satellites. Also, in the oblique impacts (< ~30°), the impactor ricochets off (Gault and Wedekind 1978). These experimental results imply that normal impacts roughly act to generate the deposits while oblique impacts act to erode the surface of the satellites.

I separate and calculate the ratio of the normal and oblique impactor flux from $E(s)$ in the Eq. 17. Then, to simplify, I assume the critical angle is 30 degree, even though this difference depends on a lot of conditions, such as surface roughness and the sizes of particles. I show the ratio of the oblique and total impactor flux in Fig. 30. The erosional effect is seems to be so strong on the leading and trailing hemisphere.

As shown in Fig. 28, the amount of the impactor flux per unit area is good agreement with the locations of the dark terrain. Also, as shown in Fig. 30, the region where the erosional effect is stronger is consistent with the region where appears the deficiency of the dark terrain. According to Fig 28, ring particles are expected to somehow deposit on other terrains, even leading or trailing side. However, strong erosions also occur on the leading and trailing side due to the oblique impacts, which may prohibit the formation of the dark terrain. Therefore, this result implies that JE-ring particles deposit on the near and far side and erode the surface regolith on the leading and trailing side.
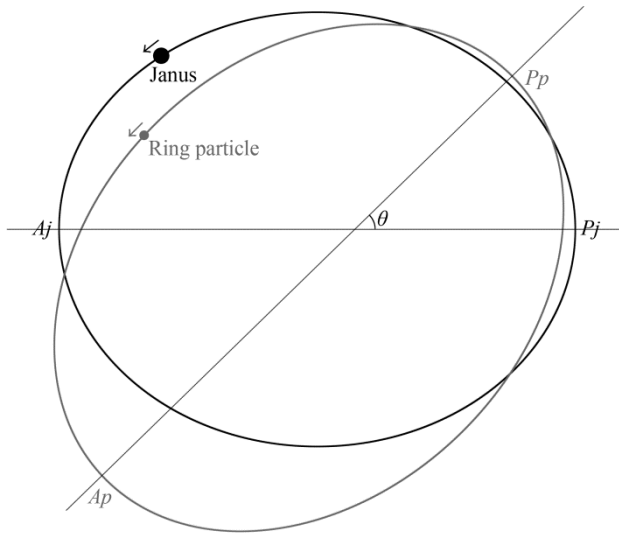
Figure 21 The conceptual figure of the orbits of a ring particle.
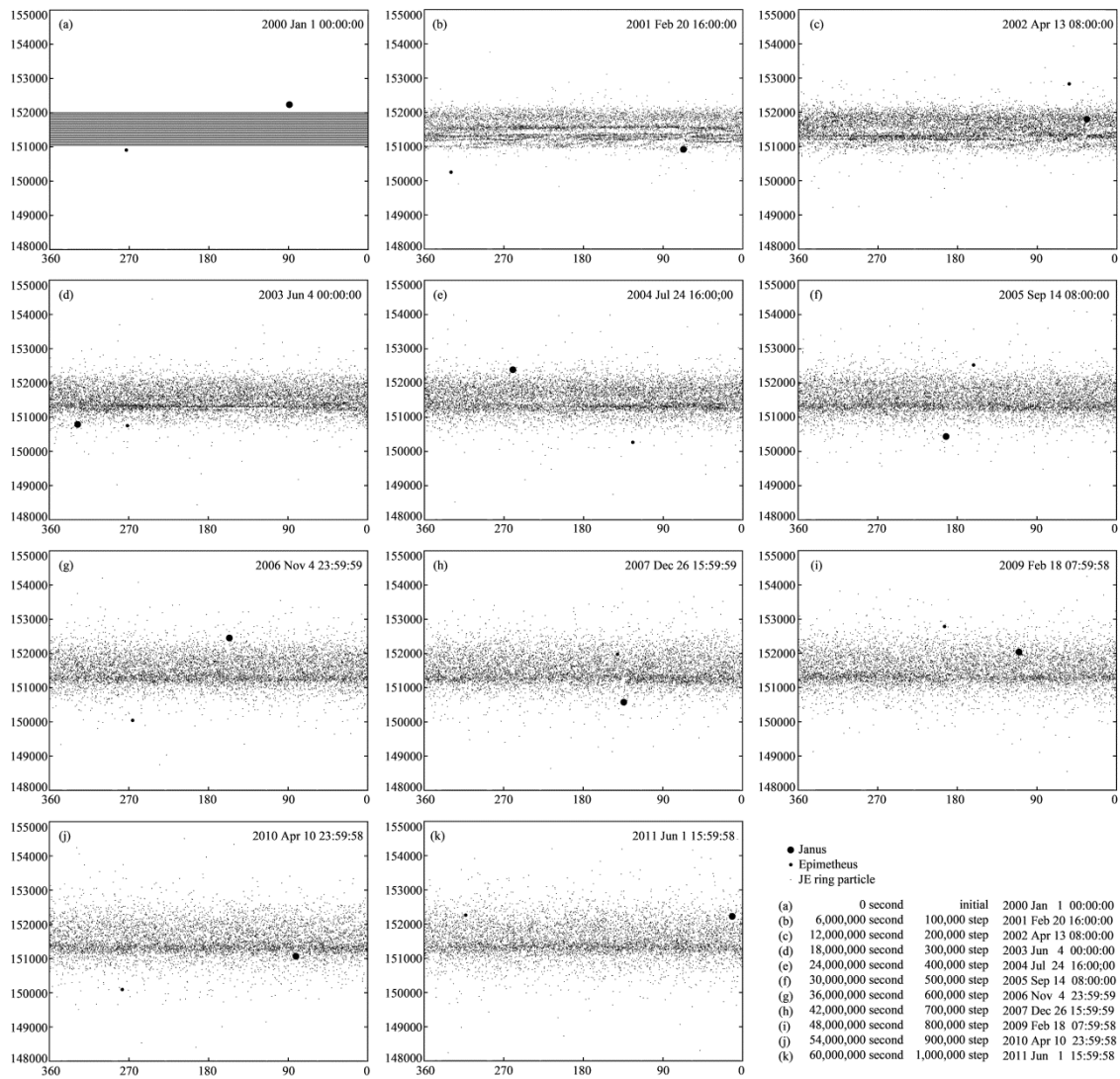I define the focus of the orbit of Janus for the center of this coordinate system (see text).

Figure 22 The fate of JE-ring particles

The fate of JE-ring particles with the initial semi-major axis ranging from 151,000 to 152,000 km. Dots represent the locations of Janus (large dots), Epimetheus (mid-sized dots), and ring particles (small dots) in the step ranging from 0 to 1,000,000. Vertical values mean the distance from the center of Saturn (km) and horizontal values mean the longitude based on Saturn-centric equatorial coordinate system.
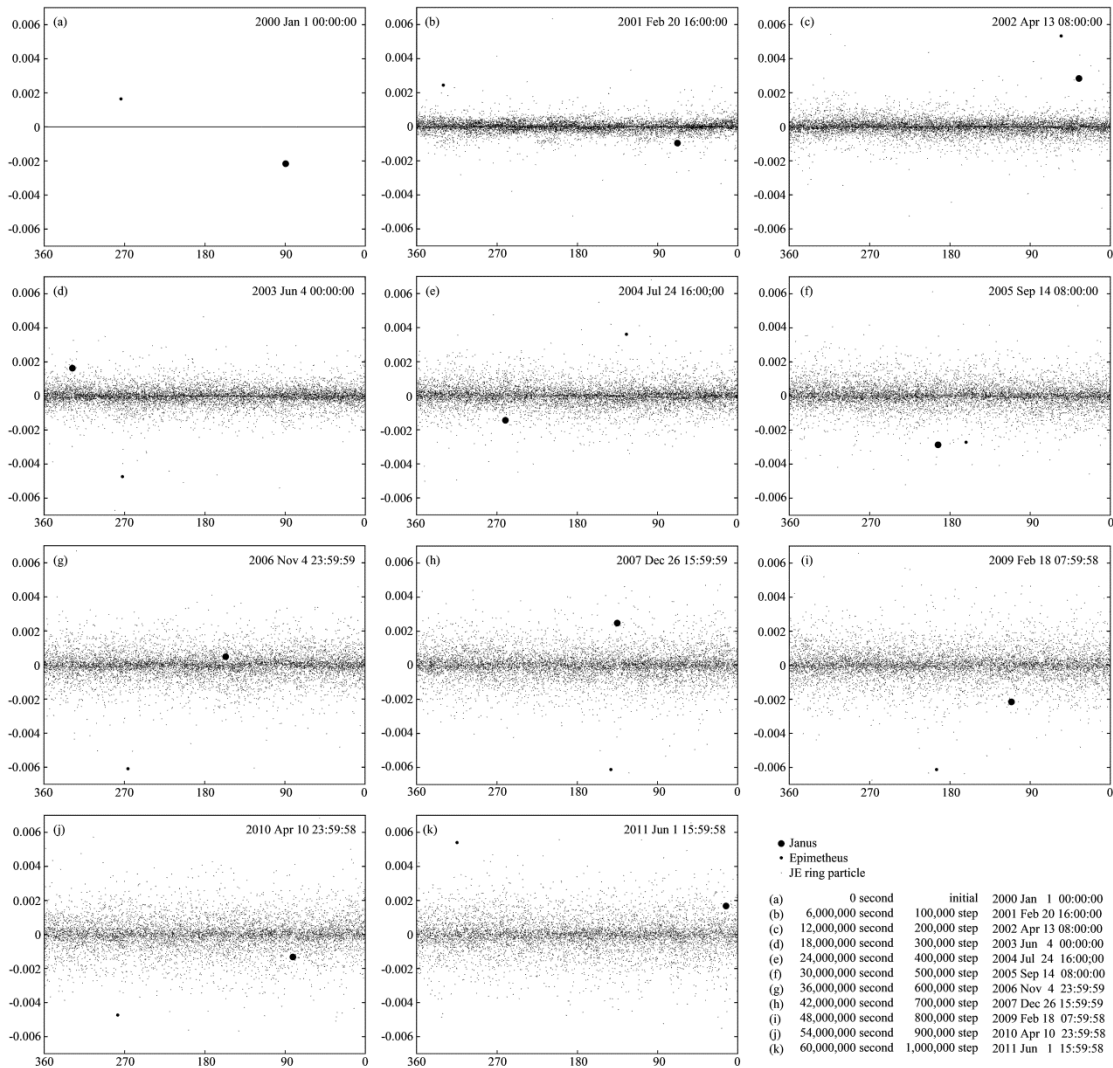
Figure 23 The fate of JE-ring particles

The fate of JE-ring particles with the initial semi-major axis ranging from 151,000 to 152,000 km. Dots represent the locations of Janus (large dots), Epimetheus (mid-size dots), and ring particles (small dots) in the step ranging from 0 to 1,000,000. Vertical and horizontal values mean the latitude and the longitude based on Saturn-centric equatorial coordinate system, respectively.
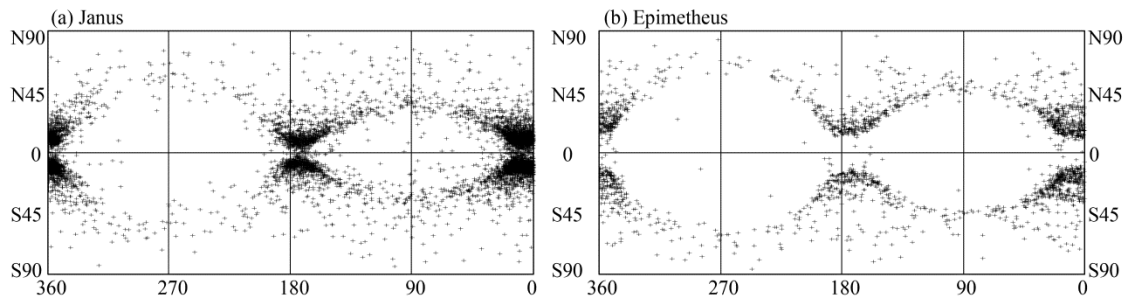
Figure 24 The direction of ring particles which collide with Janus and Epimetheus.

The longitude (vertical value) and the latitude (horizontal value) of these directions are shown in the geocentric coordinate system of the satellite.
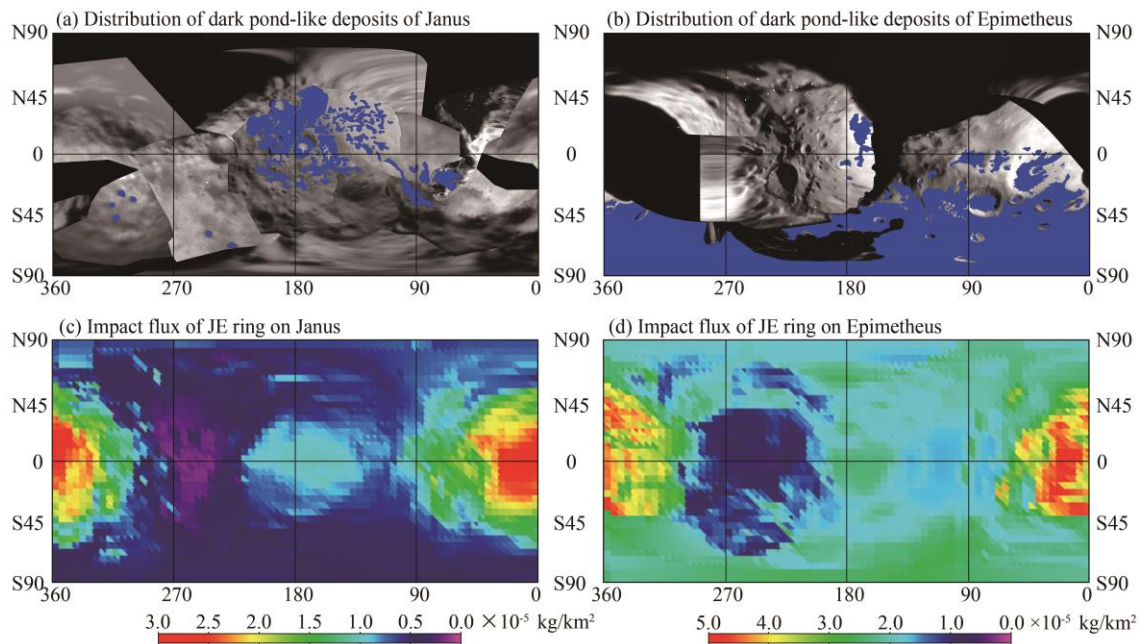

Figure 25 Impact flex on satellites.

(a) and (b) are the same as the Fig. 2c and 2d, respectively. The relative amounts per unit area of impactors supplied from JE-ring material on (c) Janus and (d) Epimetheus. This result is not considering the erosional rate. As shown in this images, blue regions of (a) and (b) are good agreement with the dense part of (c) and (d).
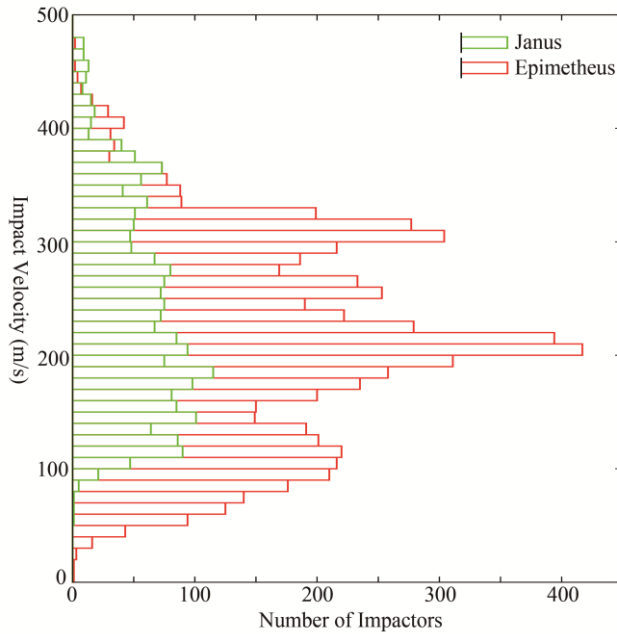
Figure 29 The distribution of impactors' velocity based on my simulation. Vertical bin is 10 m/s and horizontal value means the number of impactors within the bin. Almost all impactors have a few time larger velocities than the escape velocities of the satellites.
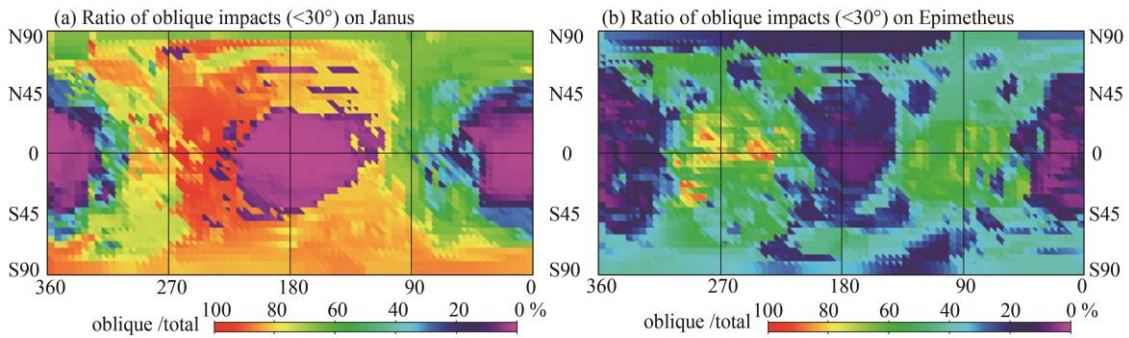

Figure 26 The ratios of the normal and oblique impactor flux.
I assume the critical angle is 30 degree. This image represents the ratio of erosional effect and depositional effect.

4. Discussion

The source of JE-ring is expected to be Janus and Epimetheus because the ring appears in the vicinity of the satellites. At the same time, the lifetime of ring particles due to the collision to the satellites is also quite short, as well as a decade (Williams and Murray 2011), which implies that the satellites continuously supply the materials to the ring. Seismic accelerations induced by large impacts may form a ring, however, this effect is temporary. Dust escape due to the electrostatic force cannot be expected because the dense plasma from Enceladus prohibits the surface electric charge (Hirata and Miyamoto 2012). Therefore, the erosion due to the collisions with JE-ring particles sustains the most part of sources of JE-ring itself. Then, my numerical result (Fig. 29) shows that almost all impactors have a few time larger velocities than the escape velocities of the satellites, which indicates that ejecta after impacts is expected to be difficult to escapes. Perhaps, the oblique impacts, which can erode the satellites, have a role to maintain the ring.

The escapement of large particles should be more difficult than that of fine particles, which indicates that the typical size of ring particles become fine. This phenomenon can explain that the dark terrain contains larger amount of fine particles than the bright terrains do. In the case of asteroids, electrostatic forces or grain dynamics are pointed to play an important role to the sorting processes. Instead, Janus and Epimetheus system may represent the bodies where sorting processes due to the orbital dynamics occur. On the other hand, fine particles on the surface and in the ring may be effectively influenced by the van der Waals force and the Lorenz forces, respectively. I note that the effects need to be examined if particles in the ring or on the surface are much smaller than 1µm.

Appendix

Because the cylindrical projection map is made by the shape models of satellites, I first estimate the shape model of satellites. The entire surface of Janus, except for sub-Saturn side and north polar region, is imaged by Cassini, which enable us to develop the local shape model of the imaged regions through the epipolar geometric method. I follow the previously proposed method (Hartley and Zisserman 2004), as well as section 2.1 in Part 1. Then, I use 25 high-resolution images shown in Table 6. As a result, I obtained the exact locations of 300 control points. On the other hand, the imaged regions of Epimetheus are limited to either the trailing side or the south polar region, which is not sufficient to develop the shape model. Therefore, I assume the simple ellipsoid for the shape of Epimetheus. By matching the shape model and an image, I can adapt every pixels of the image to a geographic coordinate of the satellite. Then, I project the brightness of these pixels to a local cylindrical projection image. Using 13 images of Janus and 4 images of Epimetheus, I can obtain the cylindrical image of satellites (Fig. 23a, b).

Conclusions

I studied geological features to discuss the origin and evolution of Saturn's small satellites. I started with an overview of the available Cassini ISS or VIMS images by 2013. In detail, I carefully examine 272 images for Janus and Epimetheus, 1,500 images for Pan and Atlas, and 500 images for Helene, Calypso, Telesto, Methone, and Pallene. I scrutinize all of these images to understand the surface conditions of the small satellites. Especially, I develop shape models of Helene and Janus for a critical evaluation of the distribution of craters or other geological features. Moreover, I calculate the local gravitational gradients for the entire surface. Also, I describe my new geological observations of Atlas, Janus, and Helene and propose a new theory to explain my findings.

I newly identify a crater on the unusually smooth-looking surface of a small saturnian satellite, Atlas. The identification implies that some sort of crater-erasing process has been active on the surface of Atlas. Atlas, which has the enigmatic shape and the ring rubble pile structure, appears the unusually smooth surface, which remained unexplained. No other small bodies are known to have an unusually smooth surface, such as Atlas. The surface of Atlas is likely covered by fine particles supplied from the A-ring of Saturn. The particles accumulate at the equatorial region of Atlas and form its enigmatic saucer-like shape. The upper-most layer of the fine particles become electro-statically unstable and migrate as a result of dust levitation, which has previously been regarded as a minor surface process on the Moon and asteroids. The particle migrations and deposits provide an unusual smoothness of the surface of Atlas. This, as well as continuity in the smoothness between the equatorial ridge and the bumpy polar region suggests the existence of similarly-sized cores. Atlas may represent the first-recognized body where resurfacing is dominated by dust levitation. I conclude Atlas's surface is formed by the existence of the source of a large amount of dusty particles, rings, and satellites of A-ring region are located at inner saturnian magnetosphere characterized by lower electron density and cooler electron

temperature, which cause dust levitation on the surface of satellites of A-ring region. As a result, these different environments cause the different surface features between satellites of A-ring regions and satellites of F-ring regions.

I identify that Janus and Epimetheus have bright and dark terrains, whose appearances are similar in terms of color, albedo, and surface feature. These data imply that the dark terrain is made of fine particle. The dark terrain on Janus appears on equatorial regions of near and far side while those on Epimetheus appear on the south polar region. The distribution may be explained by the transportation of surface materials between Janus and Epimetheus via the ring system. Also, erosion due to impacts of ring particles has a role to maintain the ring for a long time.

Based on high-resolution images, I examine the shape, the crater density, and global geological features of Helene. From the shape model, I show the north pole is located within the large depression, which makes the present rotation axis of Helene maintain the most stable state. From the crater density, I identify three distinct regions based on the crater densities, such as heavily cratered terrain (the sub-Saturn side of the trailing hemisphere), moderately cratered terrain (the anti-Saturn side of the trailing hemisphere), and less cratered terrain (the leading hemisphere). Alternatively, large craters (> 5 km) appear uniformly in any terrain. High density of globally distributed large craters and numerous small craters of the trailing hemisphere indicate Helene is a quite old object, at least 1.0 Gy. I find the nature of the leading hemisphere is explained by accumulation of the E-ring material. In detail, the accumulation causes the deficiency of small craters and the gravity-induced mass-movement process on the leading hemisphere of Helene, which forms numerous streaky depressions on a slope. The gravity plays an important role despite of the extremely tiny gravity of Helene, which may indicate that the mass-movement could be a substantial surface process even on other Solar System small bodies, such as comets and asteroids. As well as Helene, the E-ring material accumulates on other small satellites in the E-ring, such as Telesto, Calypso, Methone, and

Pallene. Telesto and Calypso appear global smooth surface and their shapes are close to sphere, compared to Helene. These features can be explained by a difference of both the amount and orbital elements of the E-ring particles as well as Tethys. Pallene and Methone are also strongly accumulated by the E-ring material. Their spherical shapes can be considered as a result of its originally irregular shape having been buried by the E-ring material.

Overall, I conclude that the interaction between satellites and ring materials dominates surface processes on the small satellites, which makes small satellites have unique features. Thus, small satellites may record a ring system. In fact, small satellites in E-ring have a clue to understand the cryovolcanism on Enceladus. Based on the crater density on Helene, the age of the E-ring deposit is between 100 My to 0.1 My. Interestingly, this view is consistent with previous proposed ages of the cryovolcanism on Enceladus.

Acknowledgements

I greatly appreciate a lot of helpful supports from Prof. Miyamoto Hideaki. He has helped me so much for last five years. Although he has been working day and night, he has spent a long time for dialogues with me. And he tells me how I should find the target, analysis data, write a paper, reply to comments by reviewers, and discuss scientific issue or whatever.

As well, Prof. James Dohm and Prof. Niihara Takahumi help me a lot. I appreciate their cooperation. Also, I appreciate to the co-author of Hirata et al. (2014), Prof. Adam Showman. They give me a lot of important comments. I acknowledge the reviewers of this doctorate thesis: Prof. Sugita Seiji, Prof. Sekine Yasuhito, Prof. Kurita Kei, Prof. Arakawa Masahiko and Prof. Ikoma Masahiro.

I appreciate to peoples in the University of Tokyo, Hemmi-kun, Hong-san, Kikuchi-san, Kiyota-san, Maeda-kun, Maruyama-san, Matsumoto-kun, Oguma-san, Peter-san, Fujii-kun, Sato-kun, Watanabe-san, and Xu-san. I'm glad to meet them and discuss with them. Also, I appreciate peoples related in this thesis. I can never thank them enough. Finally, I note that works in this thesis are supported by Grant-in-Aid for JSPS Fellows.

References

Baum, W. A., T. Kreidl, J.A. Westphal, G.E. Danielson P.K. Seidelmann, D. Pascu, D.G. Currie, 1981. Saturn's E ring: I. CCD observations of March 1980. Icarus. 47, 84-96.

Belton, M. J. S., C. R. Chapman, P. C. Thomas, M. E. Davies, R. Greenberg, K. Klaasen, D. Byrnes, L. D'Amario, S. Synnott, T. V. Johnson, A. McEwenstar, W. J. Merline, D. R. Davis, J.-M. Petit, A. Storrs, J. Veverka, B. Zellner, 1995. Bulk density of asteroid 243 Ida from the orbit of its satellite Dactyl. Nature 374, 785-788.

Buratti, B. J., J. M. Bauer, M. D. Hicks, J. A. Mosher, G. Filacchione, T. Momary, K. H. Baines, R. H. Brown, R. N. Clark, P. D. Nicholson, 2010, Cassini spectra and photometry 0.25–5.1μm of the small inner satellites of Saturn, Icarus, 206(2), 524-536.

Buratti, B. J., J. Veverka, 1984. Voyager photometry of Rhea, Dione, Tethys, Enceladus, and Mimas. Icarus. 58, 254–264.

Charnoz, S., A. Brahic, P. C. Thomas, C. C. Porco, 2007. The equatorial ridges of Pan and Atlas: terminal accretionary ornaments?, Science, 318(5856), 1622-1624.

Clark, R. N., F. P. Fanale, M. J. Gaffey, 1986. Surface composition of natural satellites. In: Burns, J. A., Matthews, M. S. (Eds.), Satellites, IAU Colloq. 77. Univ. Arizona Press, Tucson, pp.437-491.

Coates, A. J., H. J. McAndrews, A. M. Rymer, D. T. Young, F. J. Crary, S. Maurice, R. E. Johnson, R. A. Baragiola, R. L. Tokar, E. C. Sittler, G. R. Lewis, 2005. Plasma electrons above Saturn's main rings: CAPS observations. Geophy. Res. Letters 32, L14S09.

Colwell, J. E., A. A. S. Gulbis, M. Horányi, S. Robertson, 2005. Dust transport in photoelectron layers and the formation of dust ponds on Eros. Icarus 175, 159-169.

Crater Analysis Techniques Working Group, 1979. Standard Techniques for Presentation and Analysis of Crater Size-Frequency Data, Icarus, 37, 467-474.

References

Cuzzi, J., J. A. Burns, S. Charnoz, R. N. Clark, J. E. Colwell, L. Dones, L. W. Esposito, G. Filacchione, R. G. French, M. M. Hedman, S. Kempf, E. A. Marouf, C. D. Murray, P. D. Nicholson, C. C. Porco, J. Schmidt, M. R. Showalter, L. J. Spilker, J. N. Spitale, R. Srama, M. Sremčević, M. S. Tiscareno, J. Weiss, 2010. An Evolving View of Saturn's Dynamic Rings. Science 327, 1470-1475.

Cuzzi, J., R. Clark, G. Filacchione, R. French, R. Johnson, E. Marouf, L. Spilker, 2009. Ring Particle Composition and Size Distribution. In: Dougherty, M. K., Esposito, L. W., Krimigis, S. M. (Eds.), Saturn from Cassini-Huygens, Springer, New York, pp. 459-509.

Dollfus, A., 1967. PROBABLE NEW SATELLITE OF SATURN.Rep. IAU Circular 1987, International Astronomical Union, Paris.

Dones, L., C. R. Chapman, W. B. McKinnon, H. J. Melosh, M. R. Kirchoff, G. Neukum, K. J. Zahnle, 2009. Icy Satellites of Saturn: Impact Cratering and Age Determination. In: Dougherty, M. K., Esposito, L. W., Krimigis, S. M. (Eds.), Saturn from Cassini-Huygens, Springer, New York, pp. 613-635.

Doyle, L. R., L. Dones, J. N. Cuzzi, 1989. Radiative transfer modeling of Saturn's outer B ring. Icarus 80, 104-135.

Filacchione, G., F. Capaccioni, R. N. Clark, J. N. Cuzzi, D. P. Cruikshank, A. Coradini, P. Cerroni, P. D. Nicholson, T. B. McCord, R. H. Brown, B. J. Buratti, F. Tosi, R. M. Nelson, R. Jaumann, K. Stephan, 2010. Saturn's icy satellites investigated by Cassini–VIMS: II. Results at the end of nominal mission. Icarus 206, 507-523.

Filacchione, G., F. Capaccioni, R. N. Clark, P. D. Nicholson, D. P. Cruikshank, J. N. Cuzzi, J. I. Lunine, R. H. Brown, P. Cerroni, F. Tosi, M. Ciarniello, B. J. Buratti, M. M. Hedman, E. Flamini, 2013. The Radial Distribution of Water Ice and Chromophores across Saturn's System. The Astrophysical Journal. 766, 76.

Fountain, J. W., S. M. Larson, 1978. Saturn's ring and nearby faint satellites. Icarus. 36, 92–106.

References

French, R. G., P. D. Nicholson, 2000. Saturn's rings II. Particle sizes inferred from stellar occultation data. Icarus 145, 502-523.

Garrick-Bethell, I., J. W. Head III, C. M. Pieters, 2011. Spectral properties, magnetic fields, and dust transport at lunar swirls. Icarus 212, 480-492.

Gault, D. E., J. A. Wedekind, 1978, Experimental studies of oblique impact, paper presented at Lunar and Planetary Science Conference 9th, Houston, TX, March 13-17.

Gladman, B., J. J. Kavelaars, Jean-Marc Petit, Alessandro Morbidelli, Matthew J. Holman, T. Loredo, 2001. The structure of the Kuiper Belt: Size distribution and radial extent. The Astronomical Journal. 122, 1051-1066.

Gold, T., 1973. Particle interactions with celestial objects. In: Grard, R. J. L. (Ed.), Photon and Particle Interactions with Surfaces in Space. Reidel, Dordrecht, pp.571-576.

Gombosi, T. I., T. P. Armstrong, C. S. Arridge, K. K. Khurana, S. M. Krimigis, N. Krupp, A. M. Persoon, M. F. Thomsen, 2009. Saturn's Magnetospheric Configuration. In: Dougherty, M. K., Esposito, L. W., Krimigis, S. M. (Eds.), Saturn from Cassini-Huygens, Springer, New York, pp. 203-255.

Graps, A. L., G. H. Jones, A. Juhász, M. Horányi, O. Havnes, 2008. The Charging of Planetary Rings. Space Science Review 137, 435-453.

Grard, R. J. L., J. D. E. Tunaley, 1971. Photoelectron sheath near a planar probe in interplanetary space. J. Geophys. Res. 76, 2498-2505.

Gustafsson, G., J.-E. Wahlund, 2010. Electron temperatures in Saturn's plasma disc. Planetary and Space Science 58, 1018-1025.

Hamilton, D. P., J. A. Burns, 1994. Origin of Saturn's E ring: Self-Sustained, Naturally. Science. 264, 550-553.

Hartley, R., A. Zisserman, 2004. Multiple view geometry in computer vision. 2nd edition. Cambridge University Press, Cambridge, UK.

Hartmann, W. K., 1985. Impact Experiments 1. Ejecta Velocity Distributions and Related Results from Regolith Targets,

References

      Icarus, 63, 69-98.

Harzell, C. M., D. J. Scheeres, 2011. The role of cohesive forces in particle launching on the Moon and asteroids. Planetary and Space Science 59, 1758-1768.

Havnes, O., C. K. Goertz, G. E. Morfill, E. Grün, W. Ip, 1987. Dust Charges, Cloud Potential, and Instabilities in a Dust Cloud Embedded in a Plasma. J. Geophys. Res. 92, 2281-2287.

Hedman, M. M., C. D. Murray, N. J. Cooper, M. S. Tiscareno, K. Beurle, M. W. Evans, J. A. Burns, 2009. Three tenuous rings/arcs for three tiny moons. Icarus. 199, 378-386.

Hirata, N., H. Miyamoto, 2012. Dust levitation as a major resurfacing process on the surface of a saturnian icy satellite, Atlas. Icarus. 220, 106-113.

Hirata, N., H. Miyamoto, A. P. Showman, 2014. Particle deposition on the saturnian satellites from ephemeral cryovolcanism on Enceladus. Geophysical Research Letters. 41, 4135-4141.

Hirata, N., O. S. Barnouin-Jha, C. Honda, R. Nakamura, H. Miyamoto, S. Sasaki, H. Demura, A. M. Nakamura, T. Michikami, R. W. Gaskell, J. Saito, 2009. A survey of possible impact structures on 25143 Itokawa. Icarus 200, 486-502.

Horányi, M., J. A. Burns, D. P. Hamilton, 1992. The dynamics of Saturn's E ring Particles. Icarus. 97, 248-259.

Horányi, M., J. A. Burns, M. M. Hedman, G. H. Jones, S. Kempf, 2009. Diffuse Rings. In: M. Dougherty, et al., (Eds.), Saturn from Cassini-Huygens. Springer, New York, pp. 511-536.

Horányi, M., Juhász, A., Morfill, G. E., 2008. Large-scale structure of Saturn's E-ring. Geophys. Res. Lett. 35, L04203.

Howett, C. J. A., J. R. Spencer, J. Pearl, M. Segura, 2010. Thermal inertia and bolometric Bond albedo values for Mimas, Enceladus, Tethys, Dione, Rhea and Iapetus as derived from Cassini/CIRS measurements. Icarus. 206, 573-593.

Hughes, A. L., J. Colwell, A. W. DeWolfe, 2008. Electrostatic dust transport on Eros: 3D simulations of pond formation. Icarus 195, 630-648.

Ingersoll, A. P., S. P. Ewald, 2011. Total particulate mass in Enceladus plumes and mass of Saturn's E ring inferred from

References

Cassini ISS images. Icarus 216, 492-506.

Jacobson, R. A., J. Spitale, C. C. Porco, K. Beurle, N. J. Cooper, M. W. Evans, C. D. Murray, 2008. Revised Orbits of Saturn's Small Inner Satellites. The Astronomical Journal. 135, 261-263.

Jaumann, R., R. N. Clark, F. Nimmo, A. R. Hendrix, B. J. Buratti, T. Denk, J. M. Moore, P. M. Schenk, S. J. Ostro, R. Srama, 2009. Icy Satellites: Geological Evolution and Surface Processes. In: M. Dougherty, et al., (Eds.), Saturn from Cassini-Huygens. Springer, New York, pp. 637-681.

Johnson, T. V., P. R. Estrada, 2009. Origin of the Saturn System. In: Dougherty, M. K., Esposito, L. W., Krimigis, S. M. (Eds.), Saturn from Cassini-Huygens, Springer, New York, pp. 55-74.

Kargel, J. S., 2006. Enceladus: cosmic gymnast, volatile miniworld. Science. 311, 1389-91.

Kempf, S., U. Beckmann, G. Moragas-Klostermeyer, F. Postberg, R. Srama, T. Economou, J. Schmidt, F. Spahn, E. Grün, 2008. The E ring in the vicinity of Enceladus I. Spatial distribution and properties of the ring particles. Icarus 193, 420-437.

Kirchoff, M. R., P. Schenk, 2009. Crater modification and geologic activity in Enceladus' heavily cratered plains: Evidence from the impact crater distribution. Icarus. 202, 656-668.

Kirchoff, M. R., P. Schenk, 2010. Impact cratering records of the mid-sized, icy saturnian satellites. Icarus. 206, 485-497.

Lecacheux, J., P. Laques, L. Vapillon, A. Auge, R. Despiau, 1980. A new satellite of Saturn: Dione B. Icarus 43, 111-115.

Lee, P., 1996. Dust levitation on asteroids. Icarus 124, 181-194.

Marouf, E. A., G. L. Tyler, H. A. Zebker, R. A. Simpson, V. R. Eshleman, 1983. Particle size distributions in Saturn's rings from Voyager 1 radio occultation. Icarus 54, 189-211.

Matson, D. L., J. C. Castillo-Rogez, G. Schubert, C. Sotin, W. B. McKinnon, 2009. The Thermal Evolution and Internal Structure of Saturn's Mid-Sized Icy Satellites. In: M. Dougherty, et al., (Eds.), Saturn from Cassini-Huygens. Springer, New York, pp. 577-612.

McClung, D., Schaerer, P. A., 1993. The avalanche handbook.

References

Mountaineers, Seattle.

Melosh, H. J., 1989. Impact cratering: A geologic process. Oxford Univ. Press, New York.

Meyer, J., J. Wisdom, 2007. Tidal heating in Enceladus. Icarus. 188, 535-539.

Minton, D. A., 2008. The topographic limits of gravitationally bound, rotating sand piles. Icarus 195, 698-704.

Miyamoto, H., H. Yano, D. J. Scheeres, S. Abe, O. Barnouin-Jha, A. F. Cheng, H. Demura, R. W. Gaskell, N. Hirata, M. Ishiguro, T. Michikami, A. M. Nakamura, R. Nakamura, J. Saito, S. Sasaki, 2007. Regolith migration and sorting on asteroid Itokawa. Science. 316, 1011-4.

Morishima, R., L. Spilker, K. Ohtsuki, 2011. A multilayer model for thermal infrared emission of Saturn's rings. III: Thermal inertia inferred from Cassini CIRS. Icarus 215, 107-127.

Morooka, M. W., R. Modolo, J.-E. Wahlund, M. André, A. I. Eriksson, A. M. Persoon, D. A. Gurnett, W. S. Kurth, A. J. Coates, G. R. Lewis, K. K. Khurana, M. Dougherty, 2009. The electron density of Saturn's magnetosphere. Annales Geophysicae 27, 2971-2991.

Morrison, S. J., P. C. Thomas, M. S. Tiscareno, J. A. Burns, J. Veverka, 2009. Grooves on small saturnian satellites and other objects: Characteristics and significance. Icarus 204, 262-270.

Nicholson, P. D., M. M. Hedman, R. N. Clark, M. R. Showalter, D. P. Cruikshank, J. N. Cuzzi, G. Filacchione, F. Capaccioni, P. Cerroni, G. B. Hansen, B. Sicardy, P. Drossart, R. H. Brown, B. J. Buratti, K. H. Baines, A. Coradini, 2008. A close look at Saturn's rings with Cassini VIMS. Icarus 193, 182-212.

Nitter, T., O. Havnes, F. Melandsφ, 1998. Levitation and dynamics of charged dust in the photoelectron sheath above surfaces in space. J. Geophys. Res. 103, 6605-6620.

Ostro, S. J., R. D. West, L. C. Wye, H. A. Zebker, M. A. Janssen, B. Stiles, K. Kelleher, Y. Z. Anderson, R. A. Boehmer, P. Callahan, Y. Gim, G. A. Hamilton, W. T. K. Johnson, C. Veeramachaneni, R. D. Lorenz, the Cassini RADAR Team,

References

2010. New Cassini RADAR results for Saturn's icy satellites. Icarus 206, 498-506.

Porco, C. C. et al., 2005. Cassini Imaging Science: Initial Results on Saturn's Rings and Small Satellites. Science 25, 1226-1236.

Porco, C. C. et al., 2006a. Cassini observes the active south pole of Enceladus. Science. 311, 1393-401.

Porco, C. C., P. C. Thomas, J. W. Weiss, D. C. Richardson, 2007. Saturn's Small Inner Satellites: Clues to Their Origins. Science 318, 1602-1607.

Porco, C. C., the Cassini imageing Science Team, 2006b. RINGS OF SATURN (R/2006 S 1, R/2006 S 2, R/2006 S 3, R/2006 S 4)Rep. IAU Circular 8759, International Astronomical Union, Paris.

Richardson, J. E., H. J. Melosh, R. Greenberg, 2004. Impact-induced seismic shaking on asteroid 433 Eros: a surface modification process. Science 306, 1526-1529.

Roberts, J. H., F. Nimmo, 2008. Tidal heating and the long-term stability of a subsurface ocean on Enceladus. Icarus. 194, 675-689.

Salo, H., J. Schmidt, F. Spahn, 2001. Viscous overstability in Saturn's B ring. I. Direct simulations and measurement of transport coefficients. Icarus 153, 295-315.

Seidelmann, P. K., R. S. Harrington, D. Pascu, W. A. Baum, D. G. Currie, J. A. Westphal, G. E. Danielson, 1981. Saturn Satellite Observations and Orbits from the 1980 Ring Plane Crossing. Icarus 47, 282-287.

Showalter, M. R., 1991. Visual Detection of 1981 S13, Saturn's eighteenth satellite, Nature 351, 709-713.

Showman, A. P., L. Han, W. B. Hubbard, 2013. The effect of an asymmetric core on convection in Enceladus' ice shell: implications for south polar tectonics and heat flux. Geophysical Research Letters. 40, 1-5.

Smith, B. A, et al., 1981. Encounter with Saturn: Voyager 1 Imaging Science Results. Science 212, 163-191.

Smulsky, J. J., Y. J. Smulsky, 2012. Dynamic Problems of the Planets and Asteroids, and Their Discussion, International Journal of Astronomy and Astrophysics, 2(3), 129-155.

References

Spencer, J. R., A. C. Barr, L. W. Esposito, P. Helfenstein, A. P. Ingersoll, R. Jaumann, C. P. McKay, F. Nimmo, J. H. Waite, 2009. Enceladus: An Active Cryovolcanic Satellite. In: M. Dougherty, et al., (Eds.), Saturn from Cassini-Huygens. Springer, New York, pp. 683-724.

Stephan, K., R. Jaumann, R. Wagner, R. N. Clark, D. P. Cruikshank, C. A. Hibbitts, T. Roatsch, H. Hoffmann, R. H. Brown, G. Filiacchione, B. J. Buratti, G. B. Hansen, T. B. McCord, P. D. Nicholson, K. H. Baines, 2010. Dione's spectral and geological properties, Icarus, 206(2), 631-652.

Stooke, P. J., 1993, The topography of Epimetheus, Earth, Moon, and Planets, 63, 67-83.

Stooke, P. J., M. P. Lumsdon, 1993, The topography of Janus, Earth, Moon, and Planets, 62, 223-237.

Stuart, S. J., G. R. Stewart, M. C. Lewis, J. E. Colwell, M. Sremčević, 2010. Estimating the masses of Saturn's A and B rings from high-optical depth N-body simulations and steller occultations. Icarus 206, 431-445.

Sullivan, R. J., P. C. Thomas, S. L. Murchie, M. S. Robinson, 2002. Asteroid Geology from Galileo and NEAR Shoemaker Data. In: Bottke Jr., W. F., Cellino, A., Paolicchi, P., Binzel, R. P. (Eds.), Asteroids III, Univ. Arizona Press, Tucson, pp.331-350.

Thomas, P., J. A. Burns, M. Hedman, P. Helfenstein, S. Morrison, M. S. Tiscareno, J. Veverka, 2013. The inner small satellites of Saturn: A variety of worlds. Icarus. 226, 999-1019.

Tyler, G. L., E. A. Marouf, R. A. Simpson, H. A. Zebker, V. R. Eshleman, 1983. The microwave opacity of Saturn's rings at wavelengths of 3.6 and 13 cm from Voyager 1 radio occultation. Icarus 54, 160-188.

Verbiscer, A., R. French, M. Showalter, P. Helfenstein, 2007. Enceladus: Cosmic graffiti artist caught in the act. Science 315, 815.

Wahlund, J. -E., et al., 2005. The inner magnetosphere of Saturn: Cassini RPWS cold plasma results from the first encounter. Geophys. Res. Lett. 32, L20S09.

Walker, R. L., 1967. POSSIBLE NEW SATELLITE OF SATURN

Rep. IAU Circular 1991, International Astronomical Union, Paris.

Walsh, K. J., D. C. Richardson, P. Michel, 2008. Rotational breakup as the origin of small binary asteroids. Nature 454, 188-191.

Whipple, E. C., 1981. Potentials of surfaces in space. Rep. Prog. Phys. 44, 1197-1250.

Williams, G. A., C. D. Murray, 2011. Stability of co-orbital ring material with applications to the Janus–Epimetheus system. Icarus. 212, 275-293.

Willis, R. F., M. Anderegg, B. Feuerbacher, B. Fitton, 1973. Photoemission and secondary electron emission from lunar surface material. In: Grard, R. J. L. (Ed.), Photon and Particle Interaction with Surfaces in Space. Reidel, Dordrecht, pp.369-387.

Yamamoto, S., 2002. Measurement of Impact Ejecta from Regolith Targets in Oblique Impacts. Icarus. 158, 87-97.

Zahnle, K., P. Schenk, H. Levison, L. Dones, 2003. Cratering rates in the outer Solar System. Icarus. 163, 263-289.

Zebker, H. A., E. A. Marouf, G. L. Tyler, 1985. Saturn's rings—Particle size distributions for thin layer models. Icarus 64, 531-548.

Zuber, M. T., H. Y. McSween, R. P. Binzel, L. T. Elkins-Tanton, A. S. Konopliv, C. M. Pieters, D. E. Smith, 2011. Origin, Internal Structure and Evolution of 4 Vesta. Space Science Reviews 163, 77-93.